1 **Distribution and cycling of carbon monoxide in surface microlayer and**

2 **subsurface seawater in the eastern marginal seas of China**

3 Lin Yang [a, b], Peiyi Bian [a], Jing Zhang [b, c, *], Anja Engel [e], Bin Yang [a], Gui-Peng Yang [b, c, d, *]

4 [a] *Jiangsu Key Laboratory of Marine Bioresources and Environment, Jiangsu Ocean University, Lianyungang,*

5 *222005, China*

6 [b] *Frontiers Science Center for Deep Ocean Multispheres and Earth System, and Key Laboratory of Marine*

7 *Chemistry Theory and Technology, Ministry of Education, Ocean University of China, Qingdao 266100, China*

8 [c] *Laboratory for Marine Ecology and Environmental Science, Qingdao National Laboratory for Marine Science and*

9 *Technology, Qingdao 266237, China*

10 [d] *Institute of Marine Chemistry, Ocean University of China, Qingdao 266100, China*

11 [e] *GEOMAR Helmholtz Centre for Ocean Research, 24105 Kiel, Germany*

12 *Corresponding author:

13 *E-mail address:* zhangjouc@ouc.edu.cn (J. Zhang); gpyang@mail.ouc.edu.cn (G.P.

14 Yang)

15

16

19

* Corresponding authors. Key Laboratory of Marine Chemistry Theory and Technology, Ministry of Education, Ocean University of China, Qingdao 266100, China
E-mail addresses: zhangjouc@ouc.edu.cn (J. Zhang); gpyang@mail.ouc.edu.cn (G.P. Yang)

20 **Abstract**

21   Sea-surface microlayer (SML) is the boundary interface between the atmosphere

22 and ocean, exhibiting an enrichment of dissolved organic matter (DOM) and

23 participating in air-sea gas exchange. However, how do DOM enrichment in the SML

24 control the flux of several gases remains poorly understood. In our study, laboratory

25 experiments and in situ investigation in the eastern marginal seas of China were

26 conducted to determine the enrichment factors (EFs) of carbon monoxide (CO) and

27 DOM and their production and consumption rates in the SML during winter. CO,

28 chromophoric DOM (CDOM), and fluorescent DOM (FDOM) were frequently

29 enriched in the SML during winter. Although CO, CDOM and FDOM concentrations

30 decreased from in-shore regions to open ocean, higher EFs of CO and DOM in the SML

31 were generally observed in off-shore regions. Moreover, the EF of CO was lower than

32 EFs of CDOM and FDOM, which appeared to be related to the faster consumption rates

33 of CO in the SML. Considering the photoproduction rate (mean value: 12.4 nmol L^{-1} d^{-1})

34 was significantly higher than the bacteria consumption rate (mean value: 3.8 nmol L^{-1} d^{-1})

35 of CO in the SML, the EF and the concentration of CO in SML showed a large

36 diurnal variation, with the higher values observed in the early afternoon. The Flux of

37 CO exhibited a significantly negative correlation with CDOM absorption ($a_{CDOM}(254)$)

38 and fluorescence marine humic-like Component 3 in the SML, suggesting that elevated

39 DOM could stimulate the photoproduction of CO, but may also decrease air-sea CO

40 exchange in the SML.

1. Introduction

41

42   Carbon monoxide (CO) plays an important role in atmospheric chemistry (Nguyen

43 et al., 2020). It is the predominant sink of hydroxyl radical (OH•, Conte et al., 2019;

44 Nguyen et al., 2020), which oxidize pollutants and greenhouse gases (such as CH_4)

45 emitted to the atmosphere by human activities (Nguyen., 2020). The photodegradation

46 of dissolved organic matter (DOM) is thought to be the main source of CO in the ocean

47 (Stubbins et al., 2006), and ocean acts as a source of atmospheric CO (Mopper and

48 Kieber, 2002). In addition, direct production of CO by phytoplankton has been observed

49 in laboratory experiments (Gros et al., 2009) and dark/thermal production was also

50 inferred from modeling at Bermuda Atlantic Time Series (BATS, Kettle, 2005), and

51 from incubations of water samples from the Delaware Bay (Xie et al., 2005) and St

52 Lawrence estuary (Zhang et al., 2008). The first time marine production of CO by

53 macroalgae was found by Troxler et al. (1972), which was related to the occurrence of

54 bile pigments. However, direct biological production is still considered to be a minor

55 contributor to the global ocean CO budget (Fichot and Miller, 2010) and dark

56 production has been estimated to account for only 10%–32% of global ocean CO

57 production (Zhang et al., 2006). Microbial consumption and the sea-to-air fluxes

58 (Doney et al., 1995, Song et al., 2015) of CO are considered to be the main sinks of

59 oceanic CO (Zafiriou et al., 2003). CO is rapidly removed from the atmosphere

60 (lifetime of 2 months) by two major processes: geochemical oxidation by atmospheric

61 hydroxyl radicals (85%) and biological oxidation by soil microorganisms (10%)

62 (Cordero et al., 2019). With increasing concern about atmospheric pollution and the

63   potential role of CO, a primary goal of studying oceanic CO concentrations is to

64   evaluate its long-term stability and distribution trends in the marine boundary layer

65   (Conte et al., 2019; Xu et al., 2023). However, CO has not been widely studied in most

66   coastal regions over the last decade.

67   The sea surface microlayer (SML) is located at the air-sea interface and is

68   considered to play a critical role in global biogeochemical cycles and climate change

69   by regulating the air-sea exchange of relatively insoluble gases and aerosol particles

70   (Liss and Duce, 1997; Cunliffe et al., 2013). The SML has long been known as a source

71   of gels and airborne particles. For decades, articles have emphasized the presence and

72   enrichment of organic matter in the SML (Liss and Duce, 1997; Orellana et al., 2011).

73   Enrichment Factor (EF) is used to compare the properties of the SML and subsurface

74   water (SSW), and EF of a compound is defined as the ratio of the concentration in the

75   SML to that in the corresponding SSW. Higher EF values of CO and DOM in the SML

76   indicated the significant enrichment properties with respect to SSW waters. In addition,

77   SML is exposed to the most intense solar radiation of any seawater layer, especially

78   ultraviolet (UV) light, and shows significant higher colored dissolved organic matter

79   (CDOM) concentration and microbial abundances compared to the SSW (Obernosterer

80   et al., 2006; Obernosterer et al., 2008; Wurl et al., 2009; Yang et al., 2022), suggesting

81   there are more active photochemical and biochemical processes in the SML. Therefore,

82   SML contains physically, chemically, and biologically distinct environments compared

83   to the SSW (Cunliffe et al., 2011). Surfactants, are amphipathic organic substances that

84   adsorb on aquatic phase boundaries, including the air-sea interface that covers ocean's

85   surface, and mediate all mass transfer across the SML (Rickard et al., 2019 and 2022).

86   Furthermore, strong spatiotemporal gradients in gas transfer velocity (k_w) were

87   inversely correlated with natural surfactants, especially in the SML and in the

88   underlying near-surface seawater (Pereira et al., 2018). Thus, the present study aimed

89   to clarify the influence of the enrichment of DOM in the SML on sea-air CO exchange

90   by relating seawater DOM concentrations to CO emissions to the atmosphere. CDOM

91   absorption $a_{CDOM}(254)$ is an effective proxy for dissolved organic carbon (DOC) and

92   chlorophyll-*a* (Chl-*a*) concentrations in the eastern marginal seas of China (Yang et al.,

93   2021). It is purported to correspond to absorbance by relatively small, simple

94   compounds (conjugated carbon double bonds) (Lønborg et al., 2018), and it can be used

95   as an indicator for the relatively bio-labile pool of DOM (Guallar and Flos, 2019).

96   An estimated 10% of surface CO is released into the atmosphere via the sea–to-

97   air interface (Yang et al. 2024). Although intense solar radiation and enrichment of

98   DOM may promote CO photoproduction involving SML (Cunliffe et al., 2013; Pereira

99   et al., 2018; Sugai et al., 2021), and likely modifies sea-to-air gas transfer velocity (k_w)

100   of CO and other gases (Pereira et al., 2018).The role and response of the SML, along

101   with the complex interplay of biological, geochemical, and physical processes, which

102   govern the transfer of CO from the SSW, where it can either be consumed by bacteria

103   or released into the atmosphere, are much less well understood. Our study hypothesized

104   that SML specific environmental changes (i.e., enrichment processes and biochemical

105   processes) and the abundance and composition of DOM in the eastern marginal seas of

106   China influence the rate of sea-to-air CO exchange, they contribute to the formation of

107 the marine boundary layer involved in atmospheric chemistry and climate regulation.

108 Our study aimed to clarify the roles of the sea-to-air CO exchange, photochemical

109 production, and biological consumption of CO in SML ($[CO]_{sml}$) and SSW ($[CO]_{sur}$) and

110 establish a CO budget model for the marine boundary layer chemistry.

111 **2. Materials and Methods**

112 *2.1 Study Area*

113   The Yellow Sea (YS) and the East China Sea (ECS) are marginal seas of the

114 western Pacific Ocean with complicated hydrological characteristics and are

115 substantially affected by the Yellow Sea Cold Water Mass (YSCWM), the Kuroshio

116 Current, and the coastal currents (Fig. 1). The YSCWM is a low-temperature ($< 10°C$)

117 and high-salinity (32.0–33.0) water mass. Seawater in the Kuroshio presents high

118 temperatures (20–29°C), high salinities (34.2–34.8), and very low suspended

119 particulate concentrations (SPC) (< 2 mg L^{-1}) (Yang et al., 2022). Changjiang

120 River contributed more than 80% of the total freshwater inflow to the YS and the ECS

121 (Wang et al., 2020). The coastal currents are characterized by low temperatures (9–

122 24 °C), low salinities (15.0–31.5), and high SPC (> 20 mg L^{-1}). There are also

123 considerable freshwater sources draining into the coastal current areas, including the

124 Yalu River, the Changjiang River, and the Min River. Furthermore, the Changjiang

125 River Estuary (CRE) and the adjacent area are greatly affected by diluted water and

126 monsoon, with high nutrients and variable salinity distributions. In addition, the

127 atmospheric circulation in the study area was generally governed by the East Asian

128   monsoon, with strong northerly winds prevailing from September to April, and low

129   pressure over the northwestern Pacific Ocean producing offshore winds that transported

130   continental air masses into the study area (Li et al., 2019).

131   *2.2 Sampling*

132   We collected 52 paired SML and SSW water samples in the YS and ECS aboard

133   the R/V "*Dong Fang Hong 3*" from 28 December 2019 to 16 January 2020. There were

134   38 sampling stations during the daytime (7:00-19: 00) and 32 sampling stations during

135   the nighttime (19:00-7: 00). SSW samples were collected at 2–5 m depth using 24 × 10

136   L Niskin bottles mounted on a rosette equipped with a conductivity–temperature–depth

137   (CTD) profiler. SML sampling used a Garrett Screen (Garrett, 1965) (mesh: 16, wire

138   diameter: 0.36 μm; effective surface area: 2.025 cm^2) according to standard procedures

139   routine in our work (Pereira et al., 2016; Sabbaghzadeh et al., 2017). While SML

140   integrity is disrupted by a moving vessel, or when sampling from its stern (Cunliffe and

141   Wurl, 2014; Wurl et al., 2016), the SML can be successfully sampled from a vessel's

142   bow while on-station (Sabbaghzadeh et al., 2017) with the ambient waterflow toward

143   the RV (Cunliffe and Wurl, 2014). The sampling distance is at a certain distance (5 ~ 8

144   m) which the CTD sampler was deployed, and CO did not change during the sampling.

145   We therefore adopted this procedure, hand-deploying the Garrett Screen over the bow

146   on the crest of a wave (Cunliffe and Wurl, 2014) and further minimizing potential

147   contamination (engines off, wheelhouse and afterdeck downwind) (Pereira et al., 2016).

148   The SML samples were collected using the screen sampling technique (Garrett,

149   1965; Chen et al., 2016; Ma and Yang, 2023) directly off the ship's bow when

150   conditions were calm. Briefly, a screen sampler with a 1.6 mm mesh of stainless-steel

151   wire on a 40 cm × 40 cm stainless steel frame was used. The SML samples were

152   collected in 500 mL brown sample bottles. The screen was held level and dipped into

153   the sea surface, moved laterally to sample from an undisturbed film, and then

154   withdrawn slowly from the surface. Repeated dipping (11 times, 600 mL) was

155   conducted until the desired volume was collected (the depths of the SML samples

156   ranged within 100–500 μm). The screening method is often applied during field studies

157   because of its relative quickness and large sample volume compared to other techniques

158   (Chen et al., 2016). The CO in seawater samples was measured first, immediately after

159   collection. A comparison showed that screen-collected samples usually exhibit greater

160   microlayer enrichment of gas than the plate-collected samples, indicating that the

161   screen sampler might be more effective for in-situ measurements (Yang et al., 2001).

162   CDOM, DOC, and Chl-a samples were filtered using 0.7 μm glass fiber filters (GF/F,

163   Whatmann) and the filtrates were transferred to 60- and 40-mL brown glass bottles (pre-

164   cleaned and pre-combusted) for later CDOM and DOC analyses. All samples were

165   frozen (−20 °C) and protected from light. Upon arriving at the land laboratory, samples

166   were analyzed as soon as possible. Sea-surface temperature and salinity were obtained

167   from the sensors on the Seabird 911 CTD rosette. Meteorological data (e.g., wind speed

168   and air temperature) were recorded simultaneously by a ship-borne weather instrument

169   (Li et al., 2019, Table S1). The intensity of incident solar radiation was measured and

170   recorded at half-hour intervals using an OL 756 UV-visible spectroradiometer (Li et al.,

171   2020, Table S1) fitted with an OL IS-270 2-inch integrating sphere (wavelength

172   accuracy: ± 0.15 nm; wavelength repeatability: ± 0.05 nm; spectral radiance accuracy:

173   1%). Pearson's product-moment correlation was chosen to identify the relationships

174   between parameters and calculated at the confidence level of 95%.

2.3 Photoexposure experiment

176   The in-situ natural sunlight incubation experiment was conducted to estimate the

177   CO photoproduction rates in different seawater layers. SSW and SML samples for

178   photochemical incubation were collected from stations B1 and C4, as well as E2, FJ5,

179   P1, and P7, located in the YS and the ECS, respectively. SML and SSW (5 m below

180   seawater surface) samples (SSW: 2 L; SML: 500 mL) were passed through a 0.22 μm

181   PES filters (Pall Corp. Port Washington, NY, USA) immediately to remove the majority

182   of the bacteria and was then placed in an acid-washed and pre-combusted brown glass

183   bottle (2 L) in a natural sunlight incubation. Photo incubation experiments were

184   conducted on the ship immediately after sample collection. To measure the

185   photoproduction at solar radiation production rates of CO, the quartz tubes were treated

186   as follows: (1) uncovered quartz tubes exposed to full-spectrum irradiation; (2) quartz

187   tubes wrapped in multiple layers of aluminum foil to eliminate all light transmission.

188   Treatment (2) was subtracted from light-exposed treatments to remove the fraction of

189   CO produced by dark production. In addition, filtered samples from each site were

190   placed in six 80 mL optically transparent quartz tubes (acid-washed and pre-combusted)

191   and sealed without headspace or air bubbles. The quartz tubes were positioned under

192 the irradiation source to maximize the exposure of the sample; the water depth in each

193 tube was 5 cm (i.e., the diameter of the tube). Both quartz tubes (SML and SSW) were

194 irradiated for 4 hours and were exposed to direct solar irradiation while being held in a

195 water bath with circulating seawater. The change in the CO photoproduction with time

196 can be seen as a constant due to the relatively small amount of total radiation during the

197 short exposure time. The intensity of incident solar radiation was measured and

198 recorded at half-hour intervals using an OL 756 UV-visible spectroradiometer (Li et al.,

199 2020) fitted with an OL IS-270 2-inch integrating sphere (wavelength accuracy: ± 0.15

200 nm; wavelength repeatability: ± 0.05 nm; spectral radiance accuracy: 1%, Table S1).

2.4 Microbial Consumption and dark production experiments

202   Six stations were selected to determine the microbial consumption rates of CO

203 (YS: stations A1, B1 and C4; ECS: stations E2, T2 and S6). CO concentrations of

204 seawater samples were measured immediately upon collection from the SSW and the

205 SML and used as background values. Seawater was used to fill 1 L glass syringes (with

206 a 3-way nylon valve) pre-cleaned with 10% HCl-Milli-Q water and Milli-Q water until

207 headspace-free, and wrapped with Aluminum-foil. The syringes were immersed in a

208 shallow tank of flowing water which were continuously pumped from the sea in order

209 to keep the water temperature of incubation experiments to those of the ambient surface

210 seawater. Each time series of sampling consisted of 4–5 points, and the data from each

211 time series were fitted exponentially to obtain the consumption rate constant (k_{bio}).

212   Shipboard incubations were conducted to measure CO dark production rates.

213 According to Zhang et al. (2008), the dark production is the abiotic dark production.

214 Seawater was firstly filtered through 0.45 and 0.2 µm polyethersulfone membranes and

215 bubbled with CO-free gas to reduce the background CO values before being put into

216 the 1 L syringes as previously described. Then syringes were rinsed with the sample

217 water and then overflowed with the sample by 2 times their volumes before they were

218 closed without headspace. All cultures were conducted in duplicate and placed in the

219 same incubator. The water bath was completely darkened with opaque foam and black

220 garbage bags. Samples for measurement were taken from the 1 L syringes every 1–4 h

221 by syringe, taking care to evacuate the headspace after each sampling. The dark

222 production incubations were used to eliminate the effect of dark production from the

223 microbial CO consumption measurements.

224 *2.5 Determination of [CO]*

225 A TA3000R trace gas analyzer (Ametek, USA) was used to measure CO

226 concentrations in the atmosphere and seawater with a lower detection limit of 10 ppbv.

227 Before analysis, the instrument was calibrated using a CO standard gas (nominal

228 concentration: 100 ppbv in zero-grade air; analytical accuracy: ± 2%, State Center for

229 Standard Matter, China). The calibration was repeated every six hours during

230 measurements. The mixing ratio of the CO in the atmosphere was obtained by injecting

231 atmospheric samples from the gas-tight syringe directly into the instrument. The overall

232 uncertainty of the atmospheric CO measurements was estimated to be 8% at a typical

233 mixing ratio of 100 ppbv, including the contributions of instrument accuracy, carrier

234   gas, and calibration gas. CO in seawater was measured using the headspace equilibrium

235   method (Xie et al., 2002), wherein a 50 ml sample bottle was filled with seawater

236   sample and sealed (as above), and then an equivalent amount of the seawater sample

237   was replaced with 8 mL of high purity nitrogen using a gas-tight syringe. The

238   samples were then shaken at 300 r min^{-1} for 5 min to ensure that the nitrogen-filled

239   headspace in the bottle reached gas-liquid equilibrium before 6 mL of the equilibrated

240   gas was extracted using a gas-tight syringe and injected through a PTFE hydrophobic

241   filter membrane (Millipore, USA) into the TA3000R trace gas analyzer for

242   determination (the PTFE filter membranes were set up to prevent the potential entry of

243   liquid water). The measured equilibrated headspace mixing ratio of CO (ppbv) was

244   corrected using the saturated water vapor pressure and standard atmospheric pressure

245   (Stubbins et al., 2006) and then converted to obtain the concentration of dissolved CO

246   (nmol L^{-1}) in seawater (eq. 4). The method's lower detection limit was 0.02 nmol L^{-1},

247   with an analytical accuracy of better than 10%.

248   The daily fluxes (μmol m^{-2} d^{-1}) of CO in the YS and the ECS were calculated

249   using the method reported by Stubbins et al. (2006) and Yang et al. (2011), based on

250   the hourly flux (μmol m^{-2} h^{-1}). These hourly fluxes were examined on the scale of

251   individual days by plotting hourly fluxes against the time of day. Days without full

252   coverage of diurnal variations were discarded, leaving 4 d of data in the final analysis.

253   The area under each daily curve was calculated (OriginPro 8.0) to give daily CO

254   emissions.

255   The two-layer model proposed by Liss and Merlivat (1986) was used to calculate

256 the instantaneous sea-to-air flux of CO according to the following equation:

257 $$F = k([CO]_{surf} - [CO]_{eq}) \qquad (1)$$

258 where F refers to the sea-to-air flux of CO (nmol m^{-2} h^{-1}); and k is the gas transfer

259 coefficient (cm h^{-1}) as a function of wind speed u (m s^{-1}) and the Schmidt number of

260 CO (Sc). In this paper, we used empirical formula E2011 (Edson et al., 2011), which

261 applies to wind speeds from 0 to 18 m s^{-1} (Wind speed ranged from 0.68 m s^{-1} to 12.00

262 m s^{-1}), to calculate the gas transfer coefficient as follows:

263 $$k = (0.029u^3 + 5.4)(Sc/660)^{-1/2} \qquad (2)$$

264 The Schmidt number of CO was referenced from the research of Zafiriou et al.

265 (2008):

266 $$Sc = -0.0553t^3 + 4.3825t^2 - 140.07t + 2134 \qquad (3)$$

267 where t is seawater temperature (°C).

268 $[CO]_{surf}$ represents the initial concentration of CO in the surface seawater,

269 calculated by the following equation:

270 $$[CO]_{surf} = pm_a(\beta pV_w + V_a)/(RTV_w) \qquad (4)$$

271 where P is the standard atmosphere pressure (atm) and ma represents the concentration

272 of CO in the headspace when the sample reaches equilibrium. β is the Bunsen solubility

273 coefficient which is dependent on salinity and temperature (Wiesenburg and Guinasso,

274 1979). Vw and Va are the volumes of seawater and headspace in the sample bottle,

275 respectively. T is temperature (in Kelvin) and R is the gas constant with the value of

276 0.08206 atm L $(mol\ K)^{-1}$.

277 $[CO]_{eq}$ represents the concentration of CO in seawater when atmospheric CO is at

278　equilibrium with the seawater, calculated by the following equation:

279　　　　$[CO]_{eq} = ([CO]_{atm} \times \beta)/M$　　　　　　　(5)

280　where $[CO]_{atm}$ indicates the mixing ratio of CO in the atmosphere (ppbv); and M is the

281　molar volume of CO under standard pressure and temperature (25.0941 L mol^{-1}).

282　According to the error propagation equation (Nelson et al., 1998), the measurement

283　uncertainty for atmospheric CO can cause an error of 4% in calculating the sea-to-air

284　flux. Most of the error (91%) comes from the uncertainty in the gas transfer coefficient

285　(k).

286　　　The turnover time of the photochemical production (τ_{prod}) and biological

287　consumption (τ_{cons}) in the SML was calculated by the following equations (Yang et al.,

288　2005; Yang and Tsunogai, 2005;):

289　　　　　τ_{prod} = [CO] in SML / photochemical CO production rate in SML　(6)

290　　　　　$\tau_{cons} = 1/k_{CO}$ in SML　　　　　　　　　(7)

291　*2.6 Determination of CDOM absorption*

292　　　The Napierian absorption coefficients of CDOM ($a_{CDOM}(\lambda)$ (m^{-1})) were calculated

293　as follows:

294　　　　$a_{CDOM}(\lambda) = 2.303\ A_{CDOM}(\lambda)/L$　　　　　　(8)

295　where $A_{CDOM}(\lambda)$ is the absorbance of the sample at wavelength λ; and L is the cell

296　pathlength of the quartz cuvette in meters (0.1 m; Stedmon and Markager, 2003). The

297　$a_{CDOM}(254)$ (m^{-1}) was chosen to characterize CDOM abundance.

298　　　The spectral slope of the absorption spectrum was obtained by nonlinear fitting of

299　the absorption coefficient according to the following equation (Stedmon and Markager,

300　2003):

301　　　　　$a_{CDOM}(\lambda) = a_{CDOM}(\lambda_0)\exp[-S(\lambda - \lambda_0)] + K$　　　　　(9)

302　　　where $a_{CDOM}(\lambda)$ and $a_{CDOM}(\lambda_0)$ are the Napierian absorption coefficients at

303　wavelengths λ and λ_0; λ_0 is the reference wavelength; S is the spectral slope of the

304　absorption spectrum; and K represents the background parameters with CDOM

305　removed. The specific UV absorbance (SUVA$_{254}$) can be used to measure aromaticity

306　(Weishaar et al., 2003) and molecular weight (Chowdhury, 2013) of DOM, with higher

307　values generally indicative of higher aromaticity. SUVA$_{254}$ is calculated by dividing the

308　absorbance at 254 nm by DOC. Detailed Chl-*a*, DOC, fluorescence DOM (FDOM),

309　dissolved oxygen (DO), and wavelength (λ)-dependent absorption coefficients of

310　CDOM ($a_{CDOM}(\lambda)$) were determined in the laboratory using published techniques. See

311　supplementary information (Section S1) for analytical details.

312　*2.7 Enrichment factors*

313　　　The enrichment factor (EF) in the SML is defined as follows:

314　　　　　$EF = C_M/C_S$　　　　　　　　　(10)

315　　　where C_M is the concentration of any substance in the SML, and C_S is its

316　concentration in the SSW. If the EF of a substance is greater than 1.0, that substance is

317　considered enriched, and if it is less than 1.0, it is considered depleted (Chen et al.,

318　2016). Higher EF mean values of CO and DOM indicated their concentrations were

319　greater in SML than that in the SSW.

320 *2.8 Statistical analyses*

321 The correlation coefficient (r) and probability (P) values were used to evaluate the

322 goodness-of-fit. The correlation matrix, analysis of variance, and principal components

323 analysis were conducted with SPSS version 18.0 (SPSS Inc., Chicago, IL, USA) to test

324 possible relationships between the DOM parameters and environmental factors. P

325 values ≤ 0.05 were considered significant.

326 **3. Results**

327 *3.1 Environmental Factors and CO Concentration in the SSW and the SML*

328 Surface water temperature increased from 2.08 °C at YS station H12 to 23.8 °C at

329 ECS station E7 (mean value: 11.85 ± 4.53 °C, Fig. 2). Surface salinity increased from

330 28.85 at CRE station E1 to 34.62 at ECS station E7 (mean value: 32.35 ± 1.17). Wind

331 speed during sampling ranged from 0.68 m s^{-1} at station H9 to 12.00 m s^{-1} at station FJ1

332 (mean value: 6.09 ± 2.50 m s^{-1}). In recent years, bubble-mediated enhancement of the

333 transfer velocity, *k*, which exhibits a relationship with wind speed, has emerged as a

334 key issue for flux parameterization in high-wind regions (Edson et al., 2011). The

335 integrated solar irradiance (mean value: 14.09 ± 114.64 kW m^{-2}) during the in-situ

336 incubation ranged from -111.8 kW m^{-2} at YS station H5 to 417.9 kW m^{-2} at ECS station

337 F4.

338 $a_{CDOM}(254)$ in the YS (SSW: 3.59 ± 0.89 m^{-1}; SML: 4.78 ± 0.85 m^{-1}) was higher

339 than that in the ECS (SSW: 1.64 ± 0.72 m^{-1}; SML: 4.70 ± 3.35 m^{-1}) in both the SML

340   and the SSW. $a_{CDOM}(254)$ in the SML (4.74 ± 2.50 m^{-1}) showed higher values compared

341   to the SSW (2.52 ± 1.26 m^{-1}) during winter. In addition, no significant difference was

342   observed between $a_{CDOM}(254)$ in the SML and SSW (n = 52, p = 0.76, paired t-test).

343   During the study period, $[CO]_{sur}$ was particularly high at the station F4 (3.61 nmol L^{-1},

344   sampling time: 12:43) in the SML and relatively high at the station P6 (2.81 nmol L^{-1},

345   sampling time: 14:36) in the SSW (Fig. 2). The maximum $[CO]_{sml}$ was observed during

346   daytime (sampling time: 12:43, Station F4: 3.61 nmol L^{-1}), but the minimum $[CO]_{sml}$

347   was observed during night (sampling time: 22:22, Station E2: 0.59 nmol L^{-1}). No

348   significant difference was observed between [CO] in the SML (mean value: 1.54 nmol

349   L^{-1}) and the SSW (mean value: 1.23 nmol L^{-1}) (n = 52, p = 0.11, Wilcoxon signed-rank

350   test). [CO] mean value in the YS (SSW: 1.23 ± 0.40 nmol L^{-1}; SML: 1.54 ± 0.68 nmol

351   L^{-1}) were similar to the concentration observed in the ECS (SSW: 1.23 ± 0.45 nmol L^{-}

352   ^{1}; SML: 1.55 ± 0.92 nmol L^{-1}) between the SML and the SSW, respectively. The

353   stronger negative linear relationship observed between salinity and $a_{CDOM}(254)$ was

354   observed in the SSW (r = −0.716, n = 52, p < 0.01) where the influence of terrestrial

355   input in this water layer was higher than that in the SML (r = −0.038, n = 52).

356   *3.2 Variations in parallel factor analysis (PARAFAC)-derived fluorescent DOM*

357   *components and factors controlling the composition of the fluorescent components*

358   The three fluorescent DOM components were determined statistically by

359   conducting PARAFAC of the samples (Table S1; Fig. S1). Component C1 was apparent

360   with excitation and emission peaks at 275 nm and 335 nm, respectively, and was likely

361   a tryptophan-like peak T (Yamashita et al., 2017). C2 exhibited excitation/emission

362   (E_x/E_m) maxima at 350 nm/455 nm and similar to peak C derived from terrestrial humic

363   sources (Coble and Paula, 2007). Peak C has often been observed in various coastal

364   (Coble, 1996) and oceanic environments (Yamashita et al., 2017). C3 appeared as a

365   fluorophore with E_x/E_m wavelengths of 320 nm/390 nm and was similar to marine

366   humic-like components from coastal environments (Yamashita and Jaffé, 2008).

367   *3.3 Variation and enrichment of CO, CDOM, DOC, and FDOM in the SML*

368   [CO] showed relatively higher mean value in the SML, where its EFs ranged from

369   0.34 to 3.6 and it had a mean EF value of 1.3 ± 0.7 (Fig. 3). Up to 92% of CDOM

370   samples were enriched in the SML, with the average EF value of $a_{CDOM}(254)$ of 2.2 ±

371   1.2, ranging between 0.4 and 6.7. The absorption of CDOM and the fluorescence

372   intensity of FDOM components in the SML were positively correlated with their

373   respective SSW values (Fig. S2), indicating that transport of DOM from the SSW to

374   the SML is an important pathway. The EFs of CO, CDOM, and DOC in the SML were

375   generally higher in the ECS than those in the YS· (Fig. 2 and Fig. S3). The EF of C3,

376   C1 and C2 were 1.6 ± 0.7, 1.4 ± 0.6, and 1.3 ± 0.5, respectively. Furthermore, relatively

377   high CDOM absorption slope mean values ($S_{275-295}$ and S_R) were observed in the SML

378   (SSW: $S_{275-295}$: 0.0206 ± 0.0068 and S_R: 1.48 ± 0.49; SML: $S_{275-295}$: 0.0210 ± 0.0055

379   and S_R: 1.53 ± 0.22), indicating that CDOM in the SML experienced more significant

380   photodegradation than that in the SSW. The EF of CO in the daytime (mean value: 1.5

381   ± 0.8, 7:00-19:00) was 1.6 times higher than that in the nighttime (mean value: 0.9 ±

382   0.3, 19:00-7:00) (Fig. 3b)). The EF of CDOM in the daytime (mean value: 2.3 ± 11.4)

383   was 1.1 times higher than that in the nighttime (mean value: 2.1 ± 0.9) (Fig. 3b)). In

384   addition, $[CO]_{sur}$ in the daytime (mean value: 1.39 ± 0.47 nmol L^{-1}) was 1.3 times higher

385   than that in the nighttime (mean value: 1.05 ± 0.22 nmol L^{-1}) and $[CO]_{sml}$ in the daytime

386   (mean value: 1.88 ± 0.77 nmol L^{-1}) was 2.0 times higher than that in the nighttime

387   (mean value: 0.95 ± 0.29 nmol L^{-1}), likely due to CO photoproduction in the daytime.

388   *3.4 Variation of sea-to-air flux of CO*

389   The atmospheric mixing ratios ($[CO]_{atm}$) of the eastern marginal seas of China

390   ranged from 239 to 900 ppbv with an average of 602 ± 164 ppbv (n = 69; Fig. 2) during

391   winter. $[CO]_{atm}$ measured at the station A1 in the YS (the maximum concentration,

392   sampling time: 5:25) was nearly four times than that measured at the station T2 in the

393   ECS (the minimum concentration, sampling time: 21:12). YS exhibited higher CO

394   mixing ratios (mean value: 423 ppbv in 2007; mean value: 657 ppbv in 2019) than the

395   ECS (mean value: 252 ppbv in 2007; mean value: 476 ppbv in 2019) in this study and

396   a previous study (Yang et al., 2010), indicating $[CO]_{atm}$ showed relatively higher values

397   in the YS than the ECS, and $[CO]_{atm}$ showed a significant decreasing trend from the

398   northern regions to the southern regions in the eastern marginal seas of China (Fig. 2).

399   The higher $[CO]_{atm}$ at the northern stations (the YS) were representative of the

400   regionally polluted continental outflow air mass due to the anthropogenic activity in

401   East Asia.

402   The instantaneous sea-to-air fluxes of CO ranged from −1.75 to 39.78 nmol m^{-2} h^{-}

403   ^{1} in the SML (4.96 ± 7.35 nmol m^{-2} h^{-1}) and from -0.04 to 34.18 nmol m^{-2} h^{-1} in the

404   SSW (7.40 ± 7.31 nmol m^{-2} h^{-1}). Higher fluxes generally occurred in the southernmost

405   part of the survey area in the ECS (Fig. 2). Although the concentrations of $[CO]_{atm}$ in

406   the northern region were generally higher than those in the southern region, the sea-to-

407   air fluxes of CO in the SML in the ECS (6.94 ± 9.61 nmol m^{-2} h^{-1}) were 3.5 times higher

408   than that in YS (1.97 ± 2.11 nmol m^{-2} h^{-1}), indicated that $[CO]_{atm}$ did not followed the

409   sea-to-air flux of CO shown in Fig. 2. Therefore, $[CO]_{atm}$ values in the YS were heavily

410   depend on land anthropogenic input, but in the ECS, the distribution of $[CO]_{atm}$ were

411   more dependent on the sea-to-air flux of CO.

412   *3.5 CO production and consumption*

413   The photoproduction rate of CO (K_{photo}) under solar irradiance ranged from 0.708

414   to 1.05 nmol L^{-1} h^{-1} (mean $\pm$ SD: 0.860 ± 0.121 nmol L^{-1} h^{-1}) and 0.710 to 1.27 nmol L^{-1}

415   ^{1} h^{-1} (mean $\pm$ SD: 1.03 ± 0.164 nmol L^{-1} h^{-1}) during the in-situ incubation experiments

416   in the SSW and the SML, respectively, as shown in Fig. 4a) and Table 2. The mean

417   value of K_{photo} in the SML was slightly higher than that in the SSW, but the τ_{prod} was

418   lower in the SML (1.35 h) than in the SSW (1.22 h). In addition, a significant

419   relationship was observed between the light-normalized CO production rates between

420   the SML and the SSW ($r = 0.408$, $p < 0.01$, $n = 6$) during winter. The maximum k_{bio}

421   value appeared at the near-shore station B1 and the minimum value at the off-shore

422   station S6 in the SML.

423   k_{bio} in the SML and the SSW ranged between 1.43 and 3.78 d^{-1} (average $\pm$ SD:

424   2.76 ± 0.80 d^{-1}) and between 1.17 and 3.48 d^{-1} (average ± SD: 2.46 ± 0.88 d^{-1}),

425   respectively, higher than those observed in the Arctic marginal sea (mean ± SD: 0.96 ±

426   0.29 d^{-1}; Xie et al., 2005), but lower than those in the Northwest Atlantic Ocean (mean

427   ± SD: 6.24 ± 5.76 d^{-1}; Xie et al., 2005) and the China shelf sea (mean ± SD: 4.80 ± 1.82

428   d^{-1}; Zhang et al., 2019). Thus the bacterial consumption rate constant of CO was low in

429   oligotrophic open ocean regions but higher in productive coastal areas. The turnover

430   times driven by microorganism (τ_{bio}), i.e., the reciprocal of k_{bio}, were 8.9 ± 2.9 h and

431   11.9 ± 5.4 h in the SML and the SSW, respectively. Since the CO photoproduction rate

432   at the near-shore station B1 was lower than that of the near-shore station E2 and its CO

433   consumption ability was much stronger, the seawater concentration of CO at coastal

434   station E2 (SSW: 1.62 nmol L^{-1}) was higher than that at coastal station B1 (SSW: 1.51

435   nmol L^{-1}). The microbial consumption rates of CO in the SML varied greatly (average

436   of 0.18 ± 0.05 nmol L^{-1} h^{-1}), higher than the average in the SSW (0.13 ± 0.03 nmol L^{-1}

437   h^{-1}) (Fig. 4b).

438   *3.6 Primary factors controlling the distribution of the optical parameters of DOM and*

439   *CO and their EFs*

440   Negative relationships were observed between salinity and $a_{CDOM}(254)$ (SSW: p <

441   0.01, r = −0.715, n = 62; SML: p = −0.045, n = 52), $a_{CDOM}(355)$ (SSW: p < 0.01, r =

442   −0.622; SML: r = −0.146), and the C1 (SSW: p < 0.01, r = −0.758, n = 62; SML: r =

443   −0.158 , n = 52), C2 (SSW: p < 0.01, r = −0.341; SML: r = −0.106), and C3 (SSW: p <

444   0.01, r = −0.851; SML: r = −0.154) components in SSW and SML (Table 1). High and

445   low fluorescence levels of these three components were usually found at sites with low

446   and high salinities, respectively (Fig. 2). These results indicated that riverine inputs

447   mainly determined the distributions of CDOM and FDOM. Furthermore, although

448   significant CO production via CDOM photodegradation has been recorded in estuarine

449   systems (Stubbins et al., 2011), no significant relationships were observed between [CO]

450   and $a_{CDOM}(254)$ in either the SSW or the SML in our study regions. $a_{CDOM}(254)$ (p <

451   0.01, r = −0.419, n = 52) and the marine humic-like C3 (p < 0.01, r = −0.201, n = 52)

452   were both negatively correlated with the flux of CO in the SML (Fig. 5a and b). The

453   flux of CO was positively related to temperature (p < 0.01, r = 0.511, n = 62) and salinity

454   (p < 0.01, r = 0.338, n = 62) in the SSW (Fig. 5), but the EF of CO showed no significant

455   relationship with surface water temperature, salinity, or mean wind speed during

456   sampling (Fig. 5d and 5f).

4. Discussion

457

4.1 CO and DOM distribution and enrichment in the SML

458

459   The average concentration of $[CO]_{sur}$ (1.23 nmol L^{-1}) in the eastern marginal seas

460   of China was similar to that observed in the Bohai Sea and the YS during autumn

461   (Zhang et al., 2019, 1.22 nmol L^{-1}) and the Arctic waters of the Amundsen Gulf

462   (Beaufort Sea) in September/October (Xie et al., 2009, 0.17–1.34 nmol L^{-1}), but was

463   relatively lower than the Eastern Indian Ocean (Xu et al., 2023, 1.92 nmol L^{-1}). Eastern

464   Indian Ocean, on the other hand, had salinity close to 34 and the temperature was

465   relatively high (around 29°C) in autumn 2020 (Xu et al., 2023). Tropical and subtropical

466 open ocean regions were generally less affected by terrestrial influences compared to

467 estuarine, coastal and high-latitude areas. CO production and fluxes normalized to

468 discharge is generally higher in warmer waters (Kieber et al., 2014), presumably also

469 partly due to temperature controls on dissolution (Johnson et al., 1996). Therefore, the

470 relatively higher concentration of $[CO]_{sur}$ in in open ocean might be characterized by

471 the relatively high seawater temperature.

472     $[CO]_{sml}$, $[CO]_{sur}$, DOC and CDOM decreased from coastal regions to open ocean

473 and decreased from the northern sampling area (the YS) to the southern sampling area

474 (the ECS) in both the SSW and the SML (Fig. 2), which was likely due to the input

475 from the land-based sources (Yang et al., 2022). However, CO, CDOM, and FDOM

476 were more frequently enriched in the ECS (Fig. 2). Although CDOM originated from

477 allochthonous terrestrial sources in the ECS and the YS (Yang et al., 2021), CDOM in

478 the ECS was more dominated by photochemical degradation processes, while CDOM

479 in the YS was more influenced by complicated photochemical–biological coupling

480 processes (Zhu et al., 2018). $a_{CDOM}(254)$ and all three fluorescence components were

481 also positively correlated with $SUVA_{254}$ (Table 1), indicating that CDOM showed

482 higher aromaticity and humification in the eastern marginal seas of China. In addition,

483 we observed a significant positive relationship between $a_{CDOM}(254)$ and Chl-*a* in the

484 SSW ($p < 0.01$, $r = 0.333$, $n = 62$), suggesting that phytoplankton biomass and biological

485 processes played an essential role in generating new CDOM and controlling the

486 distribution of CDOM in winter. The EF of marine humic-like Component 3 was

487 significantly higher than the other fluorescence components (1.6 vs. 1.4 and

488   1.3), indicating that in-situ autochthonous DOM was more strongly enriched in the

489   SML than terrestrial DOM. Thus CO, CDOM, and FDOM were more frequently

490   enriched in the open ocean which were more attributed to the significant local

491   production.

492    $[CO]_{sur}$ and $[CO]_{sml}$, and the EFs of CO showed strong diurnal fluctuations in our

493   study (Fig. 3, Section 3.1 and 3.3). Similar diurnal fluctuations in $[CO]_{sur}$ have also

494   been observed in other areas (Ren et al., 2010; Yang et al., 2010; Yang et al., 2011),

495   likely resulting from the sunlight-induced photochemical production of CO during

496   daytime and the stronger microbial consumption at night. Significant positive

497   relationships were observed between the EFs of CO and solar irradiance (Table 3). The

498   higher EF values of CO also occurred in the daytime, suggesting that sufficient light

499   and higher temperatures combined to facilitate the photoproduction of CO and its

500   enrichment in the SML.

501   *4.2 Photochemical CO production and biological CO consumption in the SML and the*

502   *SSW*

503   The mean photoproduction rate of CO in the SML was 1.1 times higher than that

504   in the SSW in the eastern marginal seas of China, and CO in our study region showed

505   a longer turnover time than the findings of Sugai et al. (2021) in Sagami Bay, Japan

506   (τ_{prod} = 0.09 h), which is probably due to relatively low photochemical CO production

507   in the SML and stronger enrichment to long term storage of CO. The dark production

508   rates of CO (k_{dark}) ranged from −0.01 to 4.81 nmol L^{-1} d^{-1}, with a mean value of 1.25 ±

509   2.34 nmol L^{-1} d^{-1} in the SSW. Zhang et al. (2008) observed that the dark production of

510   CO exhibited a positive linear correlation with the abundance of CDOM, and terrestrial

511   DOM was more efficient at dark producing CO than marine DOM. However, no

512   significant dark production was observed in the SML water samples, which indicated

513   that dark production may be the main factor controlling CO concentrations in deeper

514   seawater.

515   The turnover times driven by sea-to-air exchange were much longer than those of

516   microbial consumption, about 219 h and 1029 h in the SSW and SML, respectively.

517   This indicated that microbial removal of CO was much faster than sea-to-air exchange,

518   which may make the latter a subordinate pathway for CO removal in our study regions.

519   The relative intense UV light at the surface ocean might influence marine microbial

520   composition and inhibit microbial consumption (Cory and Kling, 2018). However,

521   relatively higher microbial consumption rate of CO in marine systems has been

522   historically attributed to higher Chl-*a*, but lower salinity level (Xie et al., 2009; Yang et

523   al., 2010; Xu et al., 2023). In addition, the heterotrophic bacterial abundance in the SML

524   was ∼ 7.5 times greater than in the SSW and the ECS in March 2017 (Sun et al., 2020).

525   The SML is an aggregate-enriched biofilm environment with distinct microbial

526   communities, the diversity of which can differ significantly from underlying waters

527   (Liss and Duce, 2005; Cunliffe et al., 2013). This higher abundance of bacteria could

528   result in the rapid consumption of CO, along with a wide variety of other organic

529   substances in the SML. Thus the CO consumption rate in the SML and the SSW seemed

530   to be, on the whole, less affected by UV radiation. Moreover, elevated nutrient

531   concentrations can stimulate the growth of phytoplankton, biological activity, and

532   subsequently lead to the abundant production of fresh autochthonous DOM in the SML

533   (Yang et al., 2022). Therefore, compared to the SSW, the elevated DOM concentrations

534   and bacteria abundances could enhance the influences of photoproduction and

535   microbial consumption on CO cycling processes in the SML.

536   *4.3 Implications of CO sea-to-air exchange and emission to the atmosphere*

537   Based on the areas of the ECS (7.7×10^5 km^2) and YS (3.8×10^5 km^2) and their

538   respective CO sea-to-air fluxes, the releases of CO from the ECS and YS to the

539   atmosphere were estimated to range from 3 to 230 Mg CO-C month^{-1} (Mg = 10^6 g) and

540   from –0.2 to 880 Mg CO-C month^{-1}, with averages of 70 Mg CO-C month^{-1} and 10 Mg

541   CO-C month^{-1}, respectively. Clearly, the average annual release of CO to the

542   atmosphere in the ECS was much higher than (nearly 7 times) that in the YS. Yang et

543   al. (2010) suggested that the $[CO]_{sur}$ was the main factor affecting the sea–air flux of

544   CO. However, $[CO]_{sur}$ in the ECS was similar to that in the YS. As noted above, the

545   most likely sources of CO in the SML of these seas are in-situ photoproduction from

546   CDOM and/or vertical export via underlying water. Fig. 2 shows the enhanced higher

547   flux of CO observed in the SML in Changjiang Estuary matched the lowest

548   salinity concentration. Thus the fresh input of the Changjiang River and the mixing

549   processes appear to also promote the sea-to-air CO flux in the SML in the ECS than

550   that in the YS.

551   Surface-active surfactants are ubiquitous and accumulate in the uppermost < 1000

552   μm in seawater (Rickard et al., 2019), where they slow the rate of gas exchange between

553   seawater and air (Cunliffe et al., 2013). Rickard et al. (2022) observed that the first-

554   order estimates of the potential suppression of the gas transfer velocity (kw) by photo-

555   derived surfactants 12.9%–22.2% in coastal North Sea water. The highest SML

556   enrichments in surfactants have been seen in low productivity, oligotrophic regions

557   away from terrestrial influences, where surfactants concentrations in SSW are generally

558   low (Wurl et al., 2016). Pereira et al. (2018) also noted that the observed reduction in

559   the air-sea CO_2 exchange in the Atlantic Ocean was due to biological surfactants acting

560   as physical barriers and altering turbulent transfer near the water surface. Therefore, the

561   relatively lower fluxes of CO observed in the YS may be indicate seawater contains lots

562   of surfactants in the SML. Despite the clear importance of surfactants at the air-sea

563   interface, we did not conduct surfactant-specific analyses due to the analytical

564   limitations. In our experiments, the CO flux varied by 131% in winter, the negative

565   correlations between a_{CDOM}(254) and the sea-air flux of CO, and between marine

566   humic-like C3 and the sea-air flux of CO suggested that CDOM concentration may

567   reduce the CO sea-air gas exchange rate in our study regions (Fig. 5a and 5b). Therefore,

568   due to the complexity of DOM pool the SML, and its resulting decreased sea-to-air flux

569   of CO, more measurements are needed to validate our conceptual model and provide a

570   better understanding of the flux measurements of CO in the SML.

571   *4.4 Modeling of CO dynamics in the SML and the SSW*

572   All sources and sinks, including photoproduction and dark production, microbial

573   consumption and sea-air emission, should be considered in estimating CO dynamics in

574   the SML and SSW (Fig. 6). The effective solar illumination period of each day was

575   approximately 12 h, and based on this the average photoproduction rates in the SML

576   and the SSW were calculated to be 12.41 ± 1.87 nmol L^{-1} d^{-1}, 10.32 ± 1.48 nmol L^{-1} d^{-}

577   ^{1}, respectively. In the SSW, the ratio of photoproduction to dark production (1.88 ± 2.89

578   nmol L^{-1} d^{-1}) was about 4:1, and dark production accounted for about 15% of the total

579   production. No dark production of CO was observed in the SML. CO photoproduction

580   was lower in deeper water, while dark production was higher. The calculated

581   contribution of dark production to CO production in this study was similar to that for

582   the St. Lawrence estuary (14%; Zhang and Xie, 2012) but much lower than for the

583   Eastern Indian Ocean (20%; Xu et al., 2023). These were because dark production needs

584   to be given more weight in estimating its contribution to the total production of CO in

585   the deeper waters of the ocean than in estuaries (Xu et al., 2023). The total removal

586   rates of CO were about 2.64 nmol L^{-1} d^{-1} and 2.88 nmol L^{-1} d^{-1} in the SSW and the SML,

587   respectively, including the microbial consumption rates of 2.46 ± 0.88 nmol L^{-1} d^{-1} and

588   2.76 ± 0.80 nmol L^{-1} d^{-1} in the SSW and the SML, respectively. The sea-to-air exchange

589   rates were 0.18 ± 0.18 nmol L^{-1} d^{-1} in the SSW and 0.12 ± 0.18 nmol L^{-1} d^{-1} in the SML.

590   The turnover of CO occurred faster in the SML environment than in the SSW (~ 1.2

591   times). Microbial consumption was the primary sink of CO, accounting for about 95%

592   of CO removal, indicating that the biogeochemical cycling of CO is almost entirely

593   contained within seawater and only a small amount of CO is released into the

594   atmosphere (Xie et al., 2005; Yang et al., 2010; Zhang et al., 2019; Xu et al., 2023). The

28

595   production rates of CO in both SML and SSW significantly exceeds the loss rates, this

596   could lead to accumulation of CO in these systems. Therefore, CO balance in the ECS

597   and YS indicated that the underlying loss of CO (via sea-to-air flux and biodegradation)

598   was slower than the production of CO in the SML, therefore a positive CO balance was

599   maintained in the SML.

600   The average annual photoproduction, microbial consumption, and sea-to-air flux

601   of CO in the SSW were about 3.02, 1.58, and 0.04 Gg CO-C month^{-1}, respectively,

602   based on the area of the survey region ($\sim 1.2 \times 10^6$ km^2, SSW ~ 10 m). Conte et al.

603   (2019) used the NEMO-PISCES model combined with original ocean CO data

604   collected worldwide over the last 50 years, ultimately estimating that global emissions

605   of CO to the atmosphere were 4.0 Tg CO-C yr^{-1} (Tg = 10^{12} g). Based on our data, we

606   estimated the contribution of China's eastern marginal seas to global marine CO

607   emissions via sea-to-air flux to be $\sim$ 0.3‰, and the YS and the ECS occupy 2.7‰ of

608   the global ocean area. The simulated surface CO concentrations and sea-to-air fluxes

609   based on our measured values were much smaller than those simulated by Erickson

610   (1989). In our study, CO produced can be rapidly consumed by microorganisms and

611   only a small fraction was released into the atmosphere, which may explain why the

612   relative contribution of the eastern marginal seas of China to atmospheric CO was much

613   lower than the global level.

614   Notably, the enrichment of CO in the SML was more common during the daytime

615   when photochemical processes were more active, but natural sunlight can inhibit the

616   microbial consumption of CO. CO was maximal in the SML, leading to the significant

617 enrichment and supersaturation. CDOM in the SML experienced more significant

618 photodegradation than that in the SSW as can be seen in Section 3.3. Moreover,

619 researchers assumed that biological, chemical and physical processes in the SML are

620 controlled by changes in DOM concentration at this uppermost thin boundary layer

621 between the ocean and the atmosphere (Cunliffe et al., 2013). We found that

622 autochthonous humic-like DOM was more enriched in the SML than terrestrial DOM,

623 indicating that it could be an indispensable part of CO photoproduction (Yang et al.,

624 2022). Solar irradiance was positively related to the EFs of CO (Table 3), suggesting

625 that the integrated solar irradiance influenced CO enrichment in the SML. Moreover,

626 we did discover the potential for CDOM accumulation in the SML to prevent CO

627 emissions into the atmosphere (Section 4.3). Therefore, CDOM accumulation and the

628 production rates of CO in the SML significantly exceeds the loss rates, this could lead

629 to the significant accumulation of CO in the SML, especially in the daytime.

630 **5. Conclusions**

631   The present study represents the first comprehensive investigation of CO

632 distribution, loss, and production processes in both the SML and SSW, as well as sea-

633 to-air CO flux in the ECS and YS during winter. $[CO]_{sur}$, $[CO]_{sml}$, CDOM, FDOM, and

634 DOC were generally decreased from coastal regions toward open ocean. However, the

635 EFs of CO, CDOM, FDOM, and DOC were significantly higher in offshore regions,

636 suggesting that stronger enrichment processes in the SML are more prevalent in open

637 waters compared to coastal areas. CDOM absorption slope mean values ($S_{275-295}$ and

638 S_R) demonstrated that CDOM in the SML underwent more substantial

639   photodegradation than that in the SSW. Notably, the EF of the marine humic-like C3

640   was significantly higher than other fluorescence components, indicating that in-situ

641   autochthonous DOM was more strongly enriched in the SML than terrestrial DOM.

642   Significant negative correlations were observed between $a_{CDOM}(254)$ and sea-to-air CO

643   flux, as well as between sea-to-air CO flux and humic-like C3 in the SML, indicating

644   that the open sea exhibit lower CDOM concentrations but higher gas transfer

645   suppression of CO compared to nearshore waters, and that the enrichment of in-situ

646   autochthonous DOM may regulate CO emissions to the atmosphere in the SML. The

647   observed diurnal variability in CO EF led us to conclude that in-situ photoproduction

648   processes play a crucial role in determining CO distribution within the SML. Our

649   findings reveal a complex interplay between DOM enrichment and sea-air CO fluxes

650   in the SML, the connection that should be incorporated into future budget models for

651   accurate carbon cycling assessments in marine environments.

652

653   **Author contribution**

654   Lin Yang: Conceptualization, Writing-Original Draft, Writing-Review and Editing

655   Peiyi Bian: Formal analysis

656   Jing Zhang: Writing-Review and Editing, Funding acquisition

657   Anja Engel: Writing-Review and Editing

658   Bin Yang: Writing-Review and Editing

659   Gui-Peng Yang: Writing-Review and Editing, Supervision

660

Competing interests

The authors declare that they have no known competing financial interests or personal

relationships that could have appeared to influence the work reported in this paper.

Acknowledgment

References

670

671 Chen, Y., Yang, G., Xia, Q., Wu, G., 2016. Enrichment and characterization of dissolved

672   organic matter in the surface microlayer and subsurface water of the South Yellow

673   Sea. Mar. Chem. 182(Mar. 20), 1–13. doi: 10.1016/j.marchem.2016.04.001

674 Chowdhury, S., 2013. Trihalomethanes in drinking water: effect of natural organic

675   matter distribution. WATER SA, 39, 1–7. doi: 10.4314/wsa.v39i1.1

676 Coble, P.G., 1996. Characterization of marine and terrestrial DOM in seawater using

677   excitation-emission matrix spectroscopy. 51(4), 325–346. doi: 10.1016/0304-

678   4203(95)00062-3

679 Coble, P.G., Paula, G., 2007. Marine optical biogeochemistry: the chemistry of ocean

680   color. Cheminform 38(2), 402–418. doi: 10.1002/chin.200720265

681 Conte, L., Szopa, S., Séférian, R., Bopp, L., 2019. The oceanic cycle of carbon

682   monoxide and its emissions to the atmosphere. Biogeosciences, 16(4), 881–

683   902. doi: 10.5194/bg-16-881-2019

684 Cordero, P.R.F., Bayly, K., Leung, P.M., Huang, C., Greening, C., 2019. Atmospheric

685   carbon monoxide oxidation is a widespread mechanism supporting microbial

686   survival. ISME J. 13(14). doi: 10.1038/s41396-019-0479-8

687 Cory, R.M., Kling, G.W., 2018. Interactions between sunlight and microorganisms

688   influence dissolved organic matter degradation along the aquatic continuum.

689   Limnol. Oceanogr. Lett. 3(3), 102–116. doi: 10.1002/lol2.10060

690 Cunliffe, M., Engel, A., Frka, S., Gašparovi, B., Guitart, C., Murrell, J.C., Salter, M.,

691   Stolle, C., Upstill-Goddard, R., Wurl, O., 2013. Sea surface microlayers: A unified

692   physicochemical and biological perspective of the air-ocean interface. Prog.

693   Oceanogr. 109, 104–116. doi: 10.1016/j.pocean.2012.08.004

694   Cunliffe, M., Upstill-Goddard, R.C., Murrell, J.C., 2011. Microbiology of aquatic

695   surface microlayers. FEMS Microbiol. Rev. 35(2), 233–246. doi:

696   10.1111/j.1574‐6976.2010.00246.x

697   Cunliffe, M., Wurl, O., 2014. Guide to best practices to study the ocean's surface.

698   Occasional Publications of the Marine Biological Association of the United

699   Kingdom, Plymouth, UK. 118 pp.

700   Doney, S.C., Najjar, R.G., Stewart, S., 1995. Photochemistry, mixing and diurnal cycles

701   in the upper ocean. J. Mar. Res. 53(3), 341–369. doi: 10.1357/0022240953213133

702   Edson, J.B., Fairall, C.W., Bariteau, L., Zappa, C.J., Cifuentes-Lorenzen, A., Mcgillis,

703   W.R., Pezoa, S., Hare, J.E., Helmig, D., 2011. Direct covariance measurement of

704   CO_2 gas transfer velocity during the 2008 Southern Ocean Gas Exchange

705   Experiment: Wind speed dependency. J. Geophys. Res. 116(C4), 1943–1943. doi:

706   10.1029/2011jc007022

707   Engel, A., Galgani, L., 2016. The organic sea-surface microlayer in the upwelling

708   region off the coast of Peru and potential implications for air–sea exchange

709   processes. Biogeosciences 13, 989–1007. doi: 10.5194/bg-13-989-2016

710   Erickson, D.J., 1989. Ocean to atmosphere carbon monoxide flux: Global inventory

711   and climate implications. Global Biogeochem. Cyc. 3(4), 305–314. doi:

712   10.1029/GB003i004p00305

713   Fichot, C.G., Miller, W.L., 2010. An approach to quantify depth-resolved marine

714   photochemical fluxes using remote sensing: application to carbon monoxide (CO)

715   photoproduction. Remote Sens. Environ. 114, 1363–1377. doi:

716   10.1016/j.rse.2010.01.019

717   Garrett, W.D., 1965. Collection of slick-forming materials from the sea surface. Limnol.

718   Oceanogr. 10(1965), 602–605. doi: 10.2307/2833459

719   Gros, V., Peeken, I., Bluhm, K., Zöllner, E., Sarda-Esteve, R., Bonsang, B., 2009.

720   Carbon monoxide emissions by phytoplankton: evidence from laboratory

721   experiments. Environ. Chem. 6, 369–379. doi: 10.1071/EN09020

722   Guallar, C., Flos, J., 2019. Linking phytoplankton primary production and

723   chromophoric dissolved organic matter in the sea. Prog. Oceanogr. 176, 102116.

724   doi: 10.1016/j.pocean.2019.05.008

725   Johnson, J.E., Bates, T.S., 1996. Sources and sinks of carbon monoxide in the mixed

726   layer of the tropical south Pacific Ocean. Global Biogeochem. Cy. 10(2), 347–359.

727   doi: 10.1029/96GB00366

728   Kettle, A.J., 2005. Diurnal cycling of carbon monoxide (CO) in the upper ocean near

729   Bermuda. Ocean Model. 8(4), 337–367. doi: 10.1016/j.ocemod.2004.01.003

730   Kieber, D.J., Miller, G.W., Neale, P.J., Mopper, K., 2014. Wavelength and temperature-

731   dependent apparent quantum yields for photochemical formation of hydrogen

732   peroxide in seawater. Env. Sci.: Processes Impacts. doi: 10.1039/C4EM00036F.

733   Li, Y., He, Z., Yang, G.P., Wang, H., Zhuang, G.C., 2019. Volatile halocarbons in the

734   marine atmosphere and surface seawater: diurnal and spatial variations and

735   influences of environmental factors. Atmos. Environ. 214, 116820.

736   10.1016/j.atmosenv.2019.116820

737   Li, Y., Fichot, C.G., Geng, L., Scarratt, M.G., Xie, H., 2020. The Contribution of

738   Methane Photoproduction to the Oceanic Methane Paradox. Geophys. Res. Lett.

739   47(14), 1–10. doi: 10.1029/2020GL088362

740   Liss, P.S., Merlivat, L., 1986. Air-sea gas exchange rates: Introduction and synthesis.

741   In P. Buat-Ménard (Ed.), The role of air-sea exchange in geochemical cycling, (pp.

742   113–127). Dordrecht, Netherlands: Springer. Retrieved from

743   papers3://publication/uuid/BAFDE7E6-A29C-466C-B1CD-2A7DAFF930D5

744 Liss, P.S., Duce, R.A., (Eds) 1997. The sea surface and global change. Cambridge, UK:

745   Cambridge University Press.

746 Liss, P.S., Duce, R.A., 2005. The Sea Surface and Global Change, Cambridge

747   University Press, UK, ISBN-13: 978-0511525025.

748 Lønborg, C., Álvarez-Salgado, X.A., Duggan, S., Carreira, C., 2018. Organic matter

749   bioavailability in tropical coastal waters: The Great Barrier Reef. Limnol.

750   Oceanogr. 63, 1015–1035. doi: 10.1002/lno.10717

751 Ma, Q.Y., Yang, G.P., 2023. Roles of phytoplankton, microzooplankton, and bacteria in

752   DMSP and DMS transformation processes in the East China Continental Sea. Prog.

753   Oceanogr. 103003. doi: 10.1016/j.pocean.2023.103003

754 Mopper, K., Kieber, D.J., 2002. Photochemistry and cycling of carbon, sulfur, nitrogen

755   and phosphorus. In: Hansell, D.A., Carlson, C.A. (Eds.), Biogeochemistry of

756   Marine Dissolved Organic Matter. AP. doi: 10.1016/b978-012323841-2/50011-7

757 Nelson, E.D., McConnell, L.L., Baker, J.E., 1998. Diffusive Exchange of Gaseous

758   Polycyclic Aromatic Hydrocarbons and Polychlorinated Biphenyls Across the

759   Air−Water Interface of the Chesapeake Bay. Environ. Sci. Technol. 32(7), 912–

760   919. doi: 10.1021/es9706155

761 Nguyen, N.H., Turner, A.J., Yin, Y., Prather, M.J., Frankenberg, C., 2020. Effects of

762   chemical feedbacks on decadal methane emissions estimates. Geophys. Res. Lett.

763   47(3), e2019GL085706. doi: 10.1029/2019GL085706

764 Obernosterer, I., Catala, P., Reinthaler, T., Herndl, G.J., Lebaron, P., 2006. Enhanced

765   heterotrophic activity in the surface microlayer of the Mediterranean Sea. Aquat.

766   Microb. Ecol. 39, 293–302. doi: 10.3354/ame039293

767 Obernosterer, I., Catala, P., Lami, R., Caparros, J., Ras, J., Bricaud, A., Dupuy, C., van

768   Wambeke, F., Lebaron, P., 2008. Biochemical characteristics and bacterial

769   community structure of the sea surface microlayer in the South Pacific Ocean.

770   Biogeosciences, 5, 693–705. doi: 10.5194/bg-5-693-2008

771 Orellana, M.V., Matrai, P.A., Leck, C., Rauschenberg, C.D., Lee, A.M., Coz, E., 2011.

772   Marine microgels as a source of cloud condensation nuclei in the high Arctic. Proc.

773   Natl. Acad. Sci. 108, 13612–13617. doi: 10.1073/pnas.1102457108.

774 Pereira, R., Schneider-Zapp, K., Upstill-Goddard, R.C., 2016. Surfactant control of gas

775   transfer velocity along an offshore coastal transect: results from a laboratory gas

776   exchange tank. Biogeosciences, 13, 3981–3989. doi: 10.5194/bg-13-3981-2016.

777 Pereira, R., Ashton, I., Sabbaghzadeh, B., Shutler, J.D., Upstill-Goddard, R.C., 2018.

778   Reduced air–sea CO_2 exchange in the Atlantic Ocean due to biological surfactants.

779   Nat. Geosci. 11, 492–496. doi: 10.1038/s41561-018-0136-2

780 Ren, C., Yang, G., Lu, X., 2014. Autumn photoproduction of carbon monoxide in

781   Jiaozhou Bay China. J. Ocean U. China, 13(3), 428–436. doi: 10.1007/s11802-

782   014-2225-1

783 Rickard, P.C., Uher, G., Upstill-Goddard, R.C., Frka, S., Mustaffa, N.I.H., Banko-Kubis,

784 H.M., Hanne Marie, B.K., Ana Cvitesic, K., Blazenka, G., Christian, S., Oliver,

785 W., 2019. Reconsideration of seawater surfactant activity analysis based on an

786 inter-laboratory comparison study. Mar. Chem. 208, 103–111. doi:

787 10.1016/j.marchem.2018.11.012

788 Rickard, P.C., Uher, G., Upstill-Goddard, R.C., 2022. Photo-reactivity of surfactants in

789 the sea-surface microlayer and subsurface water of the Tyne estuary, UK. Geophys.

790 Res. Lett. 49(4), e2021GL095469. doi: 10.1029/2021GL095469

791 Sabbaghzadeh, B., Upstill-Goddard, R.C., Beale, R., Pereira, R., Nightingale, P.D.,

792 2017. The Atlantic Ocean surface microlayer from 50°N to 50°S is ubiquitously

793 enriched in surfactants at wind speeds up to 13 m s^{-1}. Geophys. Res. Lett. 44(6),

794 2852–2858. doi: 10.1002/2017GL072988

795 Song, G., Richardson, J.D., Werner, J.P., Xie, H., Kieber, D.J., 2015. Carbon monoxide

796 photoproduction from particles and solutes in the Delaware estuary under

797 contrasting hydrological conditions. Environ. Sci. Technol. 49(24), 14048–14056.

798 doi: 10.1021/acs.est.5b02630

799 Stedmon, C.A., Markager, S., Bro, R., 2003. Tracing dissolved organic matter in aquatic

800 environments using a new approach to fluorescence spectroscopy. Mar. Chem.

801 82(3–4), 239–254. doi: 10.1016/S0304-4203(03)00072-0

802 Stubbins, A., Uher, G., Kitidis, V., Law, C.S., Upstill-Goddard, R.C., Woodward,

803 E.M.S., 2006. The open-ocean source of atmospheric carbon monoxide. Deep-Sea

804 Res. Part II, 53, 1685–1694. doi: 10.1016/j.dsr2.2006.05.010

805 Stubbins, A., Law, C., Uher, G., Upstill-Goddard, R., 2011. Carbon monoxide apparent

806 quantum yields and photoproduction in the Tyne estuary. Biogeosciences 8, 703–

807 713. doi:10.5194/bg-8-703-2011

808   Sugai, Y., Tsuchiya, K., Shimode, S., Toda, T., 2021. Photochemical Production and

809   Biological Consumption of CO in the SML of Temperate Coastal Waters and Their

810   Implications for Air-Sea CO Exchange. J. Geophys. Res.: Oceans 125(4), 1–14.

811   doi: 10.1029/2019JC015505

812   Sun, H., Zhang, Y.H., Tan, S., Zheng, Y.F., Zhou, S., Ma, Q.Y., Yang, G.P., Todd, J.,

813   Zhang, X.H., 2020. DMSP-Producing Bacteria Are More Abundant in the Surface

814   Microlayer than Subsurface Seawater of the East China Sea. Microb. Ecol. 80,

815   350–365. doi: 10.1007/s00248-020-01507-8

816   Troxler, R.F., 1972. Synthesis of bile pigments in plants. Formation of carbon monoxide

817   and phycocyanobilin in wild-type and mutant strains of the alga, Cyanidium

818   caldarium. Biochemistry 11(23), 4235–4242. doi: 10.1021/bi00773a007

819   Tsai, W.T., Liu, K.K., 2003. An assessment of the effect of sea surface surfactant on

820   global atmosphere–ocean CO_2 flux. J. Geophys. Res.: Oceans 108, 3127. doi:

821   10.1029/2000jc000740

822   Wang, H., Sun, F., Liu, W., 2020. Characteristics of Streamflow in the Main stream of

823   Changjiang River and the Impact of the Three Gorges Dam. Catena 104498. doi:

824   10.1016/j.catena.2020.104498

825   Weishaar, J.L., Aiken, G.R., Bergamaschi, B.A., Fram, M.S., Fujii, R., Mopper, K.,

826   2003. Evaluation of specific ultraviolet absorbance as an indicator of the chemical

827   composition and reactivity of dissolved organic carbon. Environ. Sci. Technol. 37,

828   4702–4708. doi: 10.1021/es030360x

829   Wiesenburg, D.A, Guinasso, N.L., 1979. Equilibrium solubilities of methane, carbon

830   monoxide, and hydrogen in water and sea water. J. Chem. Eng. Data, 24(4), 356–

831   360. doi: 10.1021/je60083a006

832   Wurl, O., Miller, L., Röttgers, R., Vagle, S., 2009. The distribution and fate of surface-

833   active substances in the sea-surface microlayer and water column. Mar. Chem. 115,

834   1–9. doi: 10.1016/j.marchem.2009.04.007

835   Wurl, O., Stolle, C., Thuoc, C.V., Thu, P.T., Mari, X., 2016. Biofilm-like properties of

836   the sea surface and predicted effects on air-sea CO_2 exchange. Prog. Oceanogr.

837   144, 15–24. doi: 10.1016/j.pocean.2016.03.002

838   Xie, H., Andrews, S.S., Martin, W.R., Miller, J., Zafiriou, O.C., 2002. Validated

839   methods for sampling and headspace analysis of carbon monoxide in seawater.

840   Mar. Chem. 77(2), 93–108. doi: 10.1016/S0304-4203(01)00065-2

841   Xie, H., Zafiriou, O.C., Umile, T.P., Kieber, D.J., 2005. Biological consumption of

842   carbon monoxide in Delaware Bay, NW Atlantic and Beaufort Sea. Mar. Ecol.

843   Prog. Seri. 290, 1–14. doi: 10.3354/meps290001

844   Xie, H.X., Bélanger, S., 2009. Photobiogeochemical cycling of carbon monoxide in the

845   southeastern Beaufort Sea in spring and autumn. Limnol. Oceanogr. 54(1), 234–

846   249. doi: 10.4319/lo.2009.54.1.0234

847   Xu, G.B., Xu, F., Ji, X., Zhang, J., Yan., S.B., Mao, S.H., Yang, G.P., 2023. Carbon

848   monoxide cycling in the Eastern Indian Ocean. J. Geophys. Res. Oceans 128(5).

849   doi: 10.1029/2022JC019411

850   Yamashita, Y., Hashihama, F., Saito, H., Fukuda, H., Ogawa, H., 2017. Factors

851   controlling the geographical distribution of fluorescent dissolved organic matter

852   in the surface waters of the Pacific Ocean. Limnol. Oceanogr. 62(6), 2360–2374.

853   doi: 10.1002/lno.10570

854   Yamashita, Y., Jaffé, R., 2008. Characterizing the interactions between trace metals and

855   dissolved organic matter using excitation-emission matrix and parallel factor

856   analysis. Environ. Sci. Technol. 42(19), 7374–7379. doi: 10.1021/es801357h

857 Yang, G.P., Ren, C.Y., Lu, X.L., Liu, C.Y., Ding, H.B., 2011. Distribution, flux, and

858   photoproduction of carbon monoxide in the East China Sea and Yellow Sea in

859   spring. J. Geophys. Res.: Oceans 116(C2), C02001. doi: 10.1029/2010jc006300

860 Yang, G.P., Wang, W.L., Lu, X.L., Ren, C.Y., 2010. Distribution, flux and biological

861   consumption of carbon monoxide in the Southern Yellow Sea and the East China

862   Sea. Mar. Chem. 122(1–4), 74–82. doi: 10.1016/j.marchem.2010.08.001

863 Yang, L., Zhang, J., Yang, G.P., 2021. Mixing behavior, biological and photolytic

864   degradation of dissolved organic matter in the East China Sea and the Yellow Sea.

865   Sci. Total Environ. 762(6), 143164. doi: 10.1016/j.scitotenv.2020.143164

866 Yang, L., Zhang, J., Engel A., Yang, G.P., 2022. Spatio-temporal distribution,

867   photoreactivity and environmental control of dissolved organic matter in the sea-

868   surface microlayer of the eastern marginal seas of China. Biogeosciences, 19,

869   5251–5268. doi: 10.5194/bg-19-5251-2022

870 Yang, L., Gong, C.Y., Mo, X.J., Zhang, J., Yang, B., Yang, G.P., 2024. Carbon monoxide

871   in the marine atmosphere and seawater: Spatiotemporal distribution and

872   photobiogeochemical cycling. J. Geophys. Res.: Oceans, 129(8), e2024JC021286.

873   doi: 10.1029/2024JC021286

874 Zafiriou, O.C., Andrews, S.S., Wang W., 2003. Concordant estimates of oceanic carbon

875   monoxide source and sink processes in the Pacific yield a balanced global "blue-

876   water" CO budget. Global Biogeochem. Cy. 17(1), 1015–1027. doi:

877   10.1029/2001gb001638

878 Zafiriou, O.C., Xie, H., Nelson, N.B., Wang, N.W., 2008. Diel carbon monoxide cycling

879   in the upper Sargasso Sea near Bermuda at the onset of spring and in midsummer.

880   Limnol. Oceanogr. 53(2), 835–850. doi: 10.2307/40006463

881   Zhang, J., Wang, J., Zhuang, G.C., Yang G.P., 2019. Carbon monoxide cycle in the

882   Bohai Sea and the Yellow Sea: Spatial variability, sea-air exchange and biological

883   consumption in autumn. J. Geophys. Res.: Oceans 124, 4248–4257. doi:

884   10.1029/2018JC014864

885   Zhang, Y., Xie, H., 2012. The sources and sinks of carbon monoxide in the St. Lawrence

886   system. Deep-Sea Res. Part II: Topical Studies in Oceanography 81, 114–123. doi:

887   10.1016/j.dsr2.2011.09.003

888   Zhang, Y., Xie, H., Chen, G., 2006. Factors affecting the efficiency of carbon monoxide

889   photoproduction in the St. Lawrence estuarine system (Canada). Environ. Sci.

890   Technol. 40(24), 7771–7777. doi: 10.1021/es0615268

891   Zhang, Y., Xie, H., Fichot, C.G., Chen, G., 2008. Dark production of carbon monoxide

892   (CO) from dissolved organic matter in the St. Lawrence estuarine system:

893   Implication for the global coastal and blue water CO budgets. J. Geophys. Res.:

894   Oceans 113(12), 1–9. doi: 10.1029/2008JC004811

895   Zhu, W.Z., Zhang, H.H., Zhang, J., Yang, G.P., 2018. Seasonal variation in

896   chromophoric dissolved organic matter and relationships among fluorescent

897   components, absorption coefficients, and dissolved organic carbon in the Bohai

898   Sea, the Yellow Sea and the East China Sea. J. Mar. Syst. 180, 9–23. doi:

899   10.1016/j.jmarsys.2017.12.003

900

901

902 **Figure Captions**

903 **Fig. 1.** Map of sampling stations in the East China Sea and the Yellow Sea during winter. Red box

904 represented photochemical incubation experiment stations and purple rhomboid represented

905 biological consumption experiment stations

906 ■ : Stations for CO microbial consumption incubation experiments; ▲ : Stations for CO

907 photochemical production incubation experiments; ★ : Station for both CO microbial consumption

908 and photochemical production incubation experiments; ● : Stations only for seawater sampling.

909 **Fig. 2.** Distributions of CO and the marine-like fluorescence C3 in the SSW and the SML; CO in

910 the atmosphere, and the flux of CO in the SSW and the SML; and the enrichment factors of CO and

911 the marine-like fluorescence C3 in the SML, and temperature and salinity in the in the East China

912 Sea and the Yellow Sea during winter. The concentration profiles of CO in the SSW (d) resemble

913 those of CO in the SML, which is evidence for biogeochemically very stable, salt-like (conservative)

914 properties.

915 **Fig. 3.** Variations in the $[CO]_{sml}$, $[CO]_{ssw}$, $a_{CDOM}(254)$, and DOC, EFs of [CO], $a_{CDOM}(254)$, and

916 DOC with the sampling time at each station.

917 **Fig. 4.** Variations in photochemical CO production rate of CO (K_{photo}) in the SML (red) and the

918 SSW (black) (a)). Variations in microbial consumption rate constants of CO (K_{bio}) in the SML (red)

919 and the SSW (black).

920 **Fig. 5.** Correlations between the instantaneous sea-to-air fluxes of CO (Flux) in the SSW and the

921 SML with $a_{CDOM}(254)$, marine humic-like C3, wind speeds, temperature, and salinity in the East

922 China Sea and the Yellow Sea during winter.

923   **Fig. 6**. Budget model of CO transformation in the SML and the SSW in the eastern marginal seas

924   of China during winter. (The arrows represent simplified processes of CO, CDOM and bacteria in

925   the SML and the SSW. Solid arrows represent CO sources (red) or sinks (blue) processes, and CO,

926   CDOM, bacteria enrichment (black) processes. The production (red) and removal (blue) rates and

927   their individual contributions percentages represent simplified transformation processes of CO in

928   the SML and the SSW. The black percentage represent the enrichment processes of CO, CDOM and

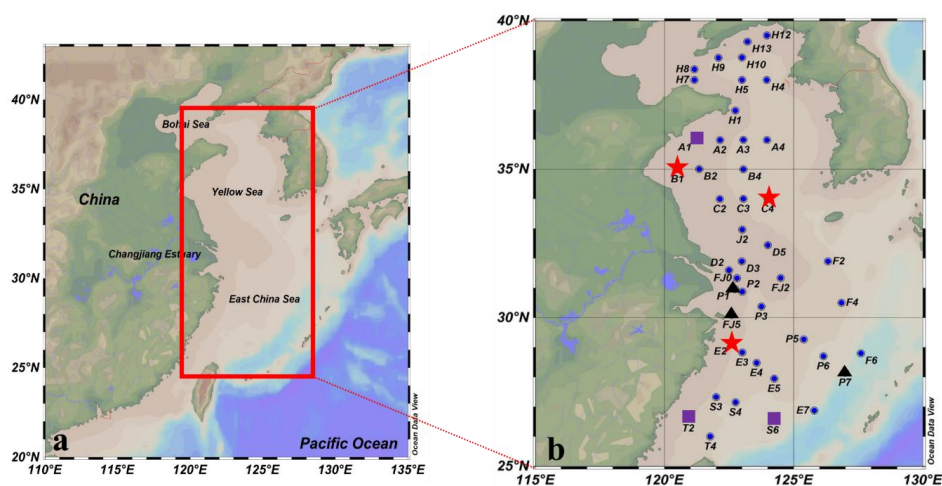929   bacteria in the SML. Bacterial enrichment was calculated by Sun et al., 2020).

Fig. 1. Map of sampling stations in the East China Sea and the Yellow Sea during winter. Red box represented photochemical incubation experiment stations and purple rhomboid represented biological consumption experiment stations.

■ : Stations for CO microbial consumption incubation experiments; ▲ : Stations for CO photochemical production incubation experiments; ★ : Station for both CO microbial consumption and photochemical production incubation experiments; ● : Stations only for seawater sampling.
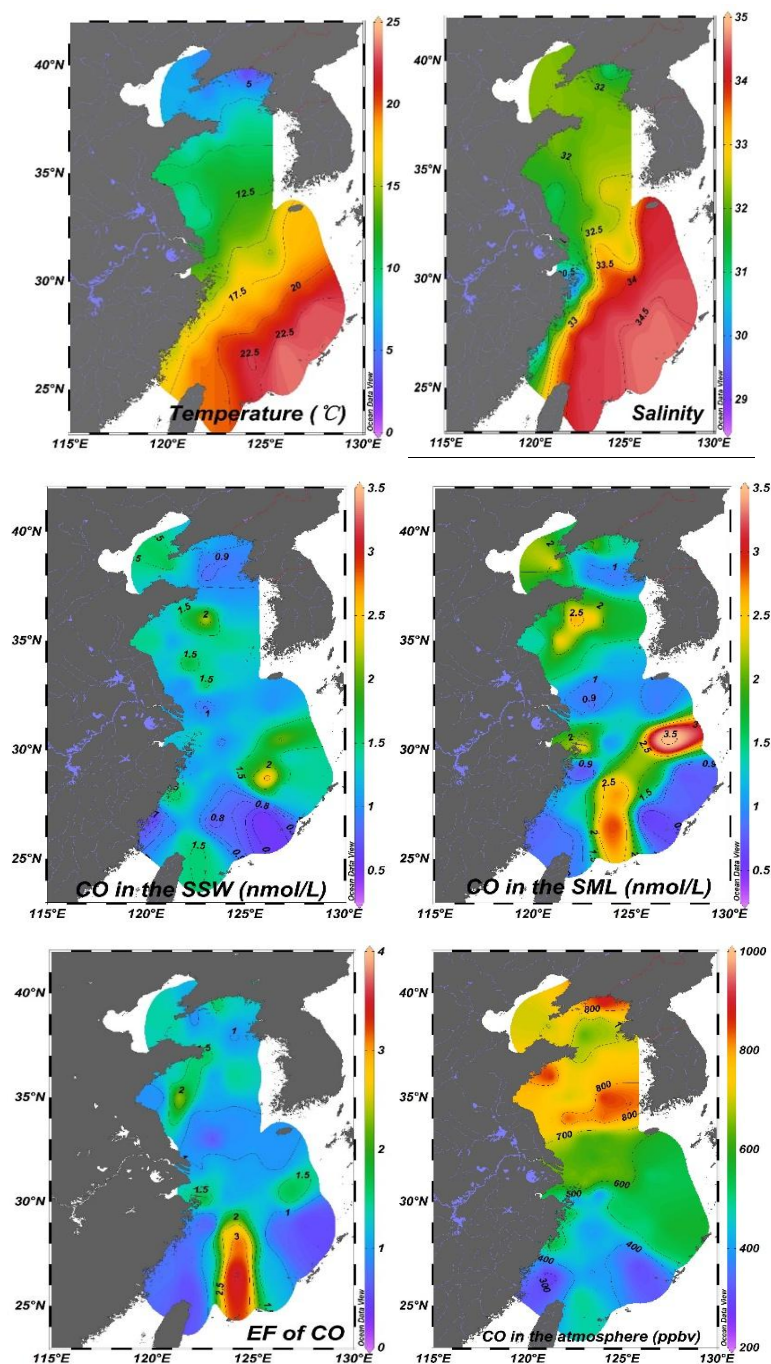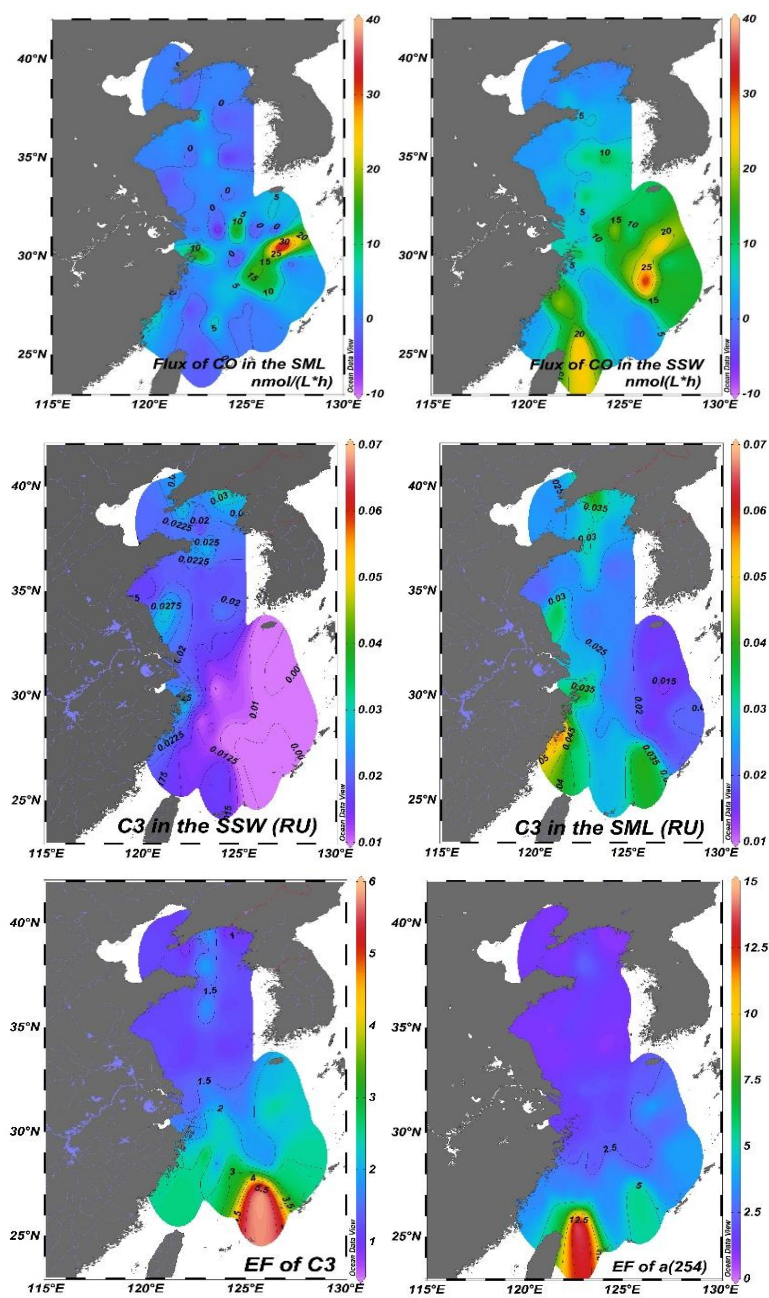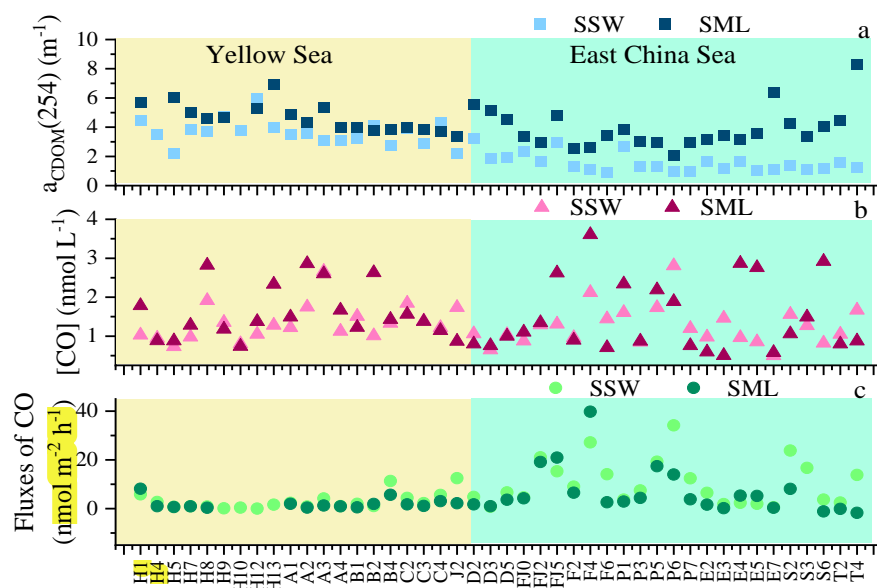
Fig. 2. Distributions of CO and the marine-like fluorescence C3 in the SSW and the SML; CO in the atmosphere, and the flux of CO in the SSW and the SML; and the enrichment factors of CO and the marine-like fluorescence C3 in the SML, and temperature and salinity in the in the East China Sea and the Yellow Sea during winter. The concentration profiles of CO in the SSW (d) resemble those of CO in the SML, which is evidence for biogeochemically very stable, salt-like (conservative) properties.
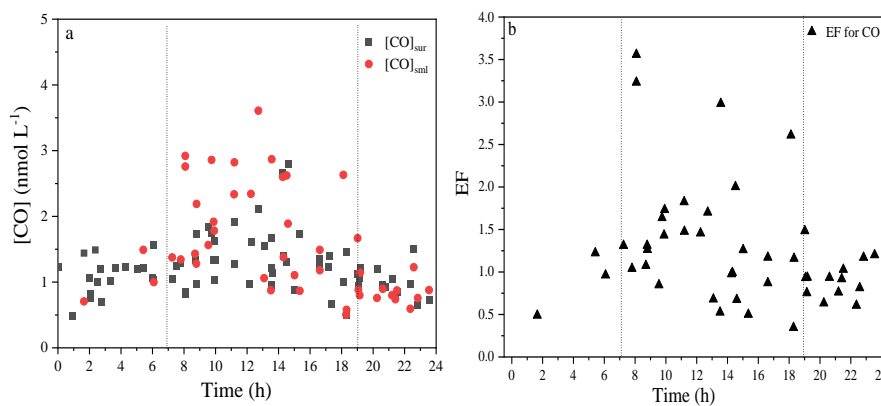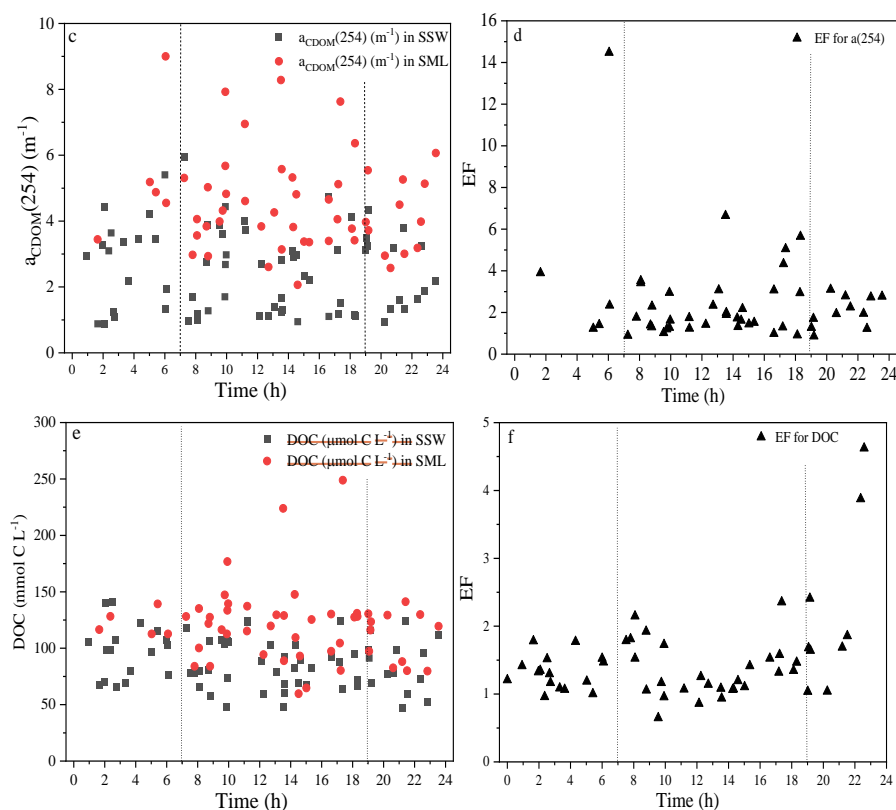
Fig. 3. Variations in the [CO]sml, [CO]ssw, aCDOM(254), and DOC, EFs of [CO], aCDOM(254), and

DOC with the sampling time at each station.
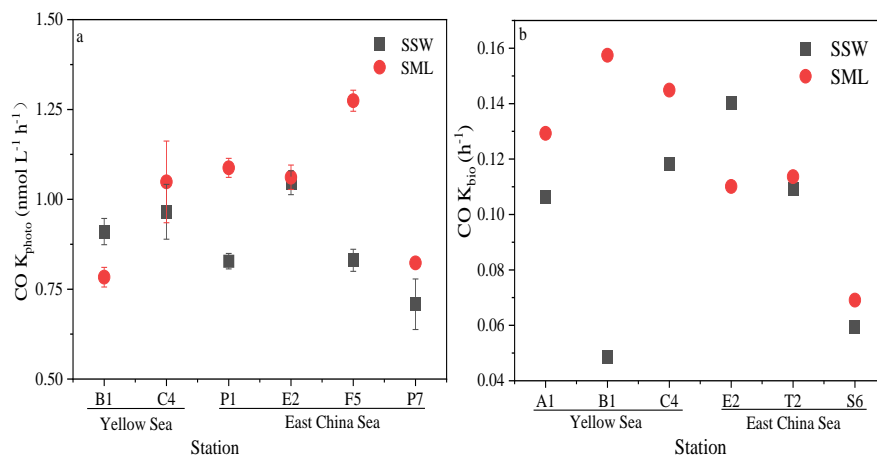
Fig. 4. Variations in photochemical CO production rate of CO (Kphoto) in the SML (red) and the

SSW (black) (a)). Variations in microbial consumption rate constants of CO (Kbio) in the SML

(red) and the SSW (black).

Fig. 5. Correlations between the instantaneous sea-to-air fluxes of CO (Flux) in the SSW and the SML with $a_{CDOM}(254)$, marine humic-like C3, wind speeds, temperature, and salinity in the East China Sea and the Yellow Sea during winter.

Fig. 6. Budget model of CO transformation in the SML and the SSW in the eastern marginal seas

of China during winter. (Bacterial enrichment was calculated by Sun et al., 2020).

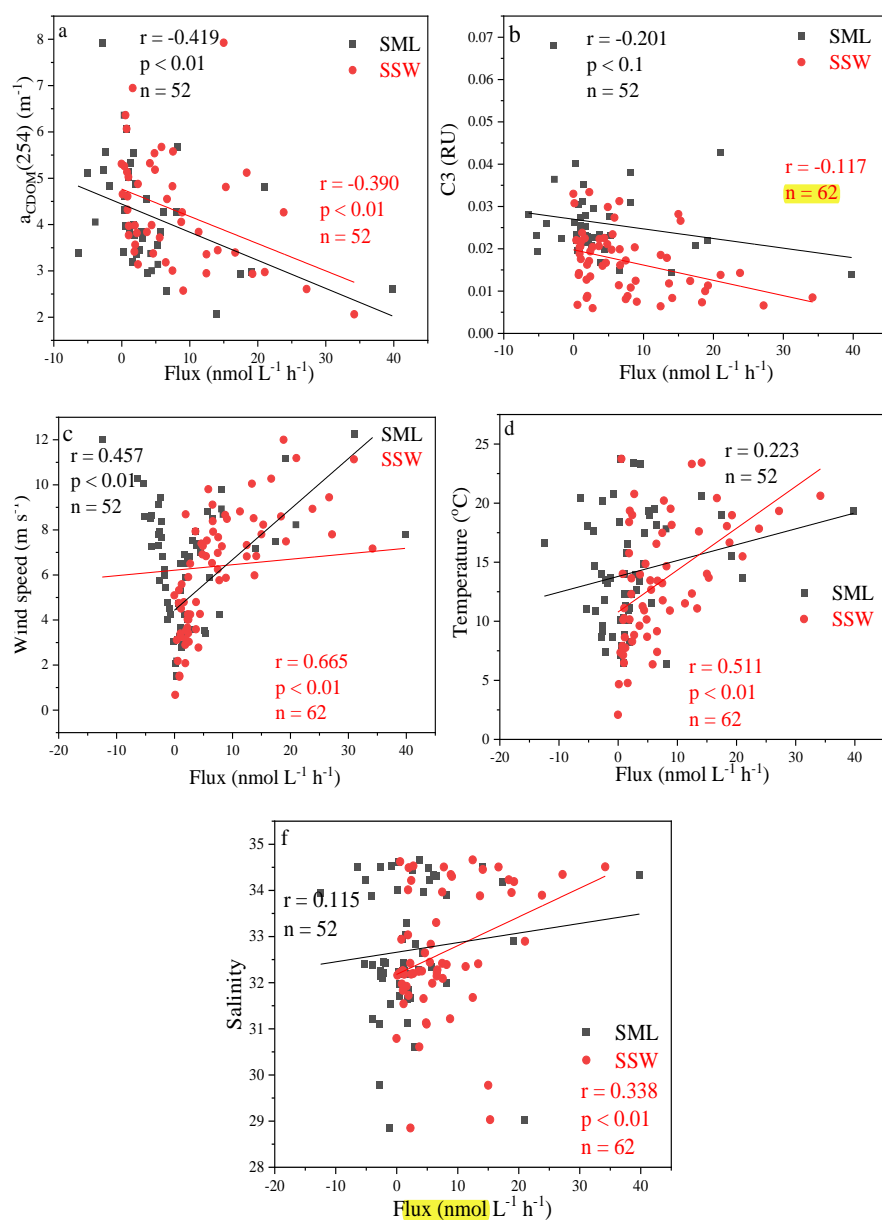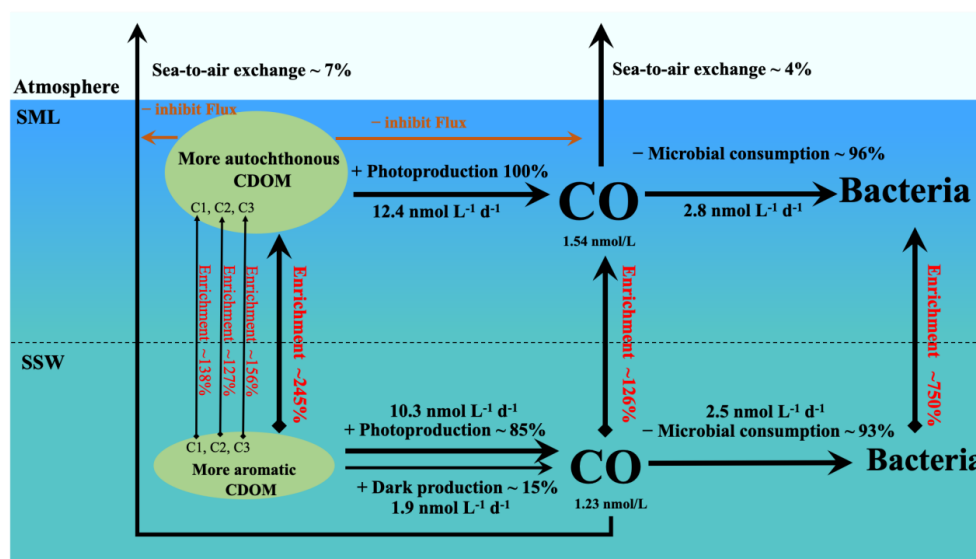Table 1 Correlation coefficients between [CO], CDOM optical parameters, DOC, Chl-a, O$_2$, salinity, and temperature in SSW a) and SML b).

a)

	[CO]$_{ssw}$	Temperature	Salinity	O$_2$	a$_{CDOM}$(254)	a$_{CDOM}$(330)	a$_{CDOM}$(355)	C1	C2	C3	DOC	Chl-a	SUVA$_{254}$	S$_{275-295}$	S$_{350-400}$
Temperature	-0.001														
Salinity	0.017	0.699**													
O$_2$	-0.072	-0.977**	-0.723**												
a$_{CDOM}$(254)	-0.029	-0.907**	**-0.716****	0.876**											
a$_{CDOM}$(330)	-0.118	-0.783**	**-0.690****	0.758**	0.939**										
a$_{CDOM}$(355)	-0.151	-0.717**	**-0.622****	0.690**	0.894**	0.990**									
C1	0.008	-0.591**	**-0.758****	0.596**	**0.675****	0.680**	0.632**								
C2	0.053	-0.324*	**-0.341****	0.286*	**0.533****	0.592**	0.599**	0.759**							
C3	-0.049	-0.788**	**-0.851****	0.779**	**0.894****	0.887**	0.838**	0.891**	0.665**						
DOC	0.008	-0.598**	-0.239	0.583**	**0.532****	0.394**	0.354**	0.241	0.146	0.323*					
Chl-a	0.109	-0.357**	-0.092	0.415**	**0.333****	0.235	0.208	0.104	0.159	0.215	0.348**				
SUVA$_{254}$	-0.081	-0.676**	-0.705**	0.654**	**0.824****	**0.860****	**0.831****	**0.653****	**0.560****	**0.853****	-0.006	0.134			
S$_{275-295}$	0.045	0.100	0.099	-0.092	-0.204	-0.385**	-0.448**	-0.197	-0.241	-0.269*	-0.009	0.084	-0.241		
S$_{350-400}$	-0.001	0.009	-0.060	0.044	-0.095	-0.214	-0.279*	0.009	-0.103	-0.043	-0.088	0.026	-0.050	0.867**	
S$_R$	0.059	0.346**	0.421**	-0.429**	-0.254*	-0.220	-0.134	-0.343**	-0.104	-0.393**	-0.087	-0.148	-0.316*	-0.506**	-0.645**

*Correlation is significant at the 0.05 level (two-tailed).

**Correlation is significant at the 0.01 level (two-tailed). N = 44.

b)

	$[CO]_{sml}$	Temperature	Salinity	SML $a_{CDOM}(254)$	SML $a_{CDOM}(330)$	SML $a_{CDOM}(355)$	SML C1	SML C2	SML C3	SML DOC	SML SUVA$_{254}$	SML S$_{275-295}$	SML S$_{350-400}$
Temperature	-0.032												
Salinity	-0.098	0.699**											
SML $a_{CDOM}(254)$	-0.137	-0.037	-0.045										
SML $a_{CDOM}(330)$	-0.119	-0.113	-0.135	0.948**									
SML $a_{CDOM}(355)$	-0.143	-0.114	-0.146	0.901**	0.989**								
SML C1	-0.095	0.158	-0.156	0.711**	0.504**	0.434**							
SML C2	-0.217	0.089	-0.106	0.670**	0.675**	0.673**	0.702**						
SML C3	-0.060	0.092	-0.154	0.823**	0.622**	0.541**	0.938**	0.703**					
SML DOC	-0.018	0.136	0.174	0.898**	0.783**	0.705**	0.572**	0.280	0.665**				
SML SUVA$_{254}$	-0.063	-0.250	-0.439**	0.136	0.303*	0.376**	0.240	0.501**	0.262	-0.272			
SML S$_{275-295}$	0.254	0.241	0.223	0.040	-0.217	-0.318*	0.323*	-0.056	0.336*	0.216	-0.409**		
SML S$_{350-400}$	0.270	0.112	0.082	0.136	-0.090	-0.187	0.385**	0.047	0.427**	0.244	-0.281	0.968**	
SML S$_R$	-0.288	0.231	0.213	-0.248	-0.057	0.044	-0.276	0.029	-0.339*	-0.296*	0.167	-0.726**	-0.776**

*Correlation is significant at the 0.05 level (two-tailed).

**Correlation is significant at the 0.01 level (two-tailed). N = 44.

Table 2 Correlation coefficients between EFs of CO, DOM absorption, DOC, three fluorescence components, temperature, salinity, and wind speed.

	EF of CO	EF of DOC	EF of $a_{CDOM}(254)$	EF of $a_{CDOM}(330)$	EF of $a_{CDOM}(355)$	EF of C1	EF of C2	EF of C3	Temperature	Salinity	Wind speed
EF of DOC	-0.098										
EF of $a_{CDOM}(254)$	-0.067	0.867**									
EF of $a_{CDOM}(330)$	-0.111	0.726**	0.912**								
EF of $a_{CDOM}(355)$	-0.124	0.556**	0.752**	0.945**							
EF of C1	0.081	0.731**	0.898**	0.753**	0.619**						
EF of C2	-0.084	0.149	0.586**	0.600**	0.580**	0.486**					
EF of C3	-0.022	0.796**	0.935**	0.830**	0.714**	0.964**	0.502**				
Temperature	0.037	0.363**	0.528**	0.533**	0.456**	0.617**	0.296*	0.604**			
Salinity	0.006	0.289*	0.478**	0.493**	0.427**	0.500**	0.268	0.491**	0.699**		
Wind speed	-0.177	0.008	0.186	0.159	0.161	-0.130	-0.006	-0.105	0.129	0.052	
Solar irradiance	0.409**	-0.024	-0.051	-0.082	-0.050	0.022	-0.139	0.002	0.160	0.157	0.104

*Correlation is significant at the 0.05 level (two-tailed).

**Correlation is significant at the 0.01 level (two-tailed). N = 44.